Bedload and suspended load contributions to breaker bar morphodynamics

Joep van Der Zanden, Dominic A. van Der A, David Hurther, Iván Cáceres, Tom O'Donoghue, Suzanne J. M. H. Hulscher, Jan S. Ribberink

Coastal Engineering 129 (2017) 74–92

Contents lists available at ScienceDirect

Coastal Engineering

journal homepage: www.elsevier.com/locate/coastaleng

Bedload and suspended load contributions to breaker bar morphodynamics

J. van der Zanden [a,*], D.A. van der A [b], D. Hurther [c], I. Cáceres [d], T. O'Donoghue [b], S.J.M.H. Hulscher [a], J.S. Ribberink [a]

[a] Department of Water Engineering and Management, University of Twente, The Netherlands
[b] School of Engineering, University of Aberdeen, United Kingdom
[c] Laboratoire des Ecoulements Géophysiques et Industriels LEGI-CNRS, University of Grenoble, France
[d] Laboratori d'Enginyeria Maritima, Universitat Politècnica de Catalunya, Spain

ARTICLE INFO

Keywords:
Breaking wave
Sheet flow
Breaker bar
Morphodynamics
Grain size sorting
Bedload transport

ABSTRACT

This study presents measurements of sheet flow processes, grain sorting, and bedload plus suspended load transport rates around a medium-sand breaker bar in a large-scale wave flume. The results offer insights in effects of wave breaking on bedload and grain sorting processes and in the quantitative contributions by bedload and suspended transport to breaker bar morphodynamics. Sheet flow layer dynamics are highly similar to observations under non-breaking waves, revealing clear effects by velocity asymmetry but no evident effects by breaking-generated turbulence, bed slope, or the cross-shore non-uniform flow. The sheet flow layer thickness can be predicted using existing empirical formulations based on local hydrodynamic forcing. At locations covering the shoaling region up to the bar crest the cross-shore variation in bedload transport rates is explained by variations in wave shape (i.e. velocity skewness and asymmetry). At locations between bar crest and bar trough, bedload transport rate magnitudes correlate positively with bed slope and turbulent kinetic energy. Bedload and suspended load transport rates are of similar magnitude but of opposite sign. Bedload transport is onshore-directed and dominates in the shoaling zone, but after wave breaking, the offshore-directed suspended sediment transport increases in magnitude and exceeds bedload transport rates in the breaking and inner surf zones. Bedload and suspended load transport contribute notably differently to bed profile evolution: bedload transfers sand grains from the offshore slope to the bar crest and additionally leads to erosion of the shoreward bar slope and deposition at the bar trough, while suspended load transport induces an opposite pattern of erosion at the bar trough and accretion at the bar crest. Grain size analysis of suspended sediment samples reveals size-selective entrainment and vertical size segregation in the inner surf zone, but suggest size-indifferent entrainment and vertical mixing by energetic vortices in the breaking region. Size-selective transport by bedload and suspended load leads to a cross-shore coarsening of the bed from shoaling to inner surf zone, with local additional sorting mechanisms around the breaker bar due to bed slope effects.

1. Introduction

Breaker bars are morphologic features that are formed naturally in wave breaking zones of dissipative and intermediate beaches (Wright and Short, 1984). Breaker bars enhance wave energy dissipation due to breaking and are one of the factors that determine the state of the beach profile (Lippmann and Holman, 1990; Wijnberg and Kroon, 2002; Price and Ruessink, 2011). Bar formation has been explained by the accumulation of shoreward sand transport under shoaling waves and offshore suspended transport under broken waves (Dyhr-Nielsen and Sorensen, 1970; Dally and Dean, 1984). Wave breaking-induced turbulent vortices may locally enhance sand suspension and offshore sand transport rates, resulting in another mechanism for bar formation (Zhang and Sunamura, 1994).

Breaker bars are dynamic and tend to migrate offshore during storm conditions, when strong wave breaking occurs, and onshore during mild wave conditions (Thornton et al., 1996; Ruessink et al., 2007). The offshore migration is attributed to an increase in both undertow velocities and suspended sediment concentrations as the intensity of wave breaking increases, which enhances offshore-directed suspended sediment transport (Sallenger et al., 1985; Thornton et al., 1996). Onshore migration is explained by the vertically and horizontally asymmetric

* Corresponding author.
E-mail address: j.vanderzanden@utwente.nl (J. van der Zanden).

http://dx.doi.org/10.1016/j.coastaleng.2017.09.005
Received 21 November 2016; Received in revised form 24 April 2017; Accepted 7 September 2017

'sawtooth' shape of the shoaled waves, leading to higher magnitudes of near-bed orbital velocities (velocity skewness) and of fluid accelerations (acceleration skewness) during the crest phase relative to the trough phase, which both favor onshore-directed wave-related sediment transport near the bed (Elgar et al., 2001; Hoefel and Elgar, 2003). Positive acceleration skewness favors onshore bedload transport as sheet flow through two processes: (i) during the relatively short-duration crest phase, the boundary layer has less time to grow, leading to a velocity gradient $du/d\zeta$ and a bed shear stress (i.e. drag force on particles) with higher crest-phase magnitudes compared to the trough phase (Nielsen, 1992; van der A et al., 2011); (ii) pressure forces, that are higher under the steep wave front than at the rear of the wave, contribute to the initial mobilization of bed grains around flow reversal (Drake and Calantoni, 2001; Calantoni and Puleo, 2006).

By including contributions of offshore-directed current-related and onshore-directed wave-related sediment transport, numerical models can predict on- and offshore bar migration reasonably well (Henderson et al., 2004; Hsu et al., 2006; Dubarbier et al., 2015; Fernández-Mora et al., 2015). However, sediment transport predictions in these models are usually only validated on bed profile evolution and may not adequately represent the individual contributions by net bedload and suspended load transport. In addition, the effects of wave breaking on sediment transport rates are not fully understood and therefore often neglected. In order to improve understanding and numerical modeling of breaker bar evolution, it is relevant to study how wave breaking affects bedload transport processes at intra-wave and wave-averaged time scales.

Previous research has shown that large-scale wave breaking enhances turbulence levels over the entire water column including the wave bottom boundary layer (van der Zanden et al., 2016). This explains observations of enhanced instantaneous bed shear stresses (Cox and Kobayashi, 2000; Sumer et al., 2013) and suspended sediment entrainment rates (Nielsen, 1984) under breaking waves. The presence of additional turbulence may also increase bedload transport rates, as shown by Sumer et al. (2003) for steady flow with artificial grid turbulence. It should be noted that the latter experiment involved mild flow conditions with a bedload transport regime that differs significantly from sheet flow conditions under full-scale breaking waves (Nielsen, 1992). Bedload in sheet flow conditions has been extensively studied in wave flumes under non-breaking waves (Dohmen-Janssen and Hanes, 2002; Schretlen, 2012) and oscillatory flow tunnels (see van der Werf et al., 2009, for an overview). Observations in the swash zone revealed that bore turbulence and cross-shore sediment advection may lead to increased sheet flow layer thicknesses compared to non-breaking wave observations (van der Zanden et al., 2015a; Lanckriet and Puleo, 2015). Due to a lack of high-resolution measurements, it is still unclear if and how wave breaking affects sheet flow transport rates and processes around the breaker bar. Consequently, it is also unclear whether existing engineering-type bedload transport formulae, used for morphodynamic simulations, should account for wave breaking effects (van Rijn et al., 2013). Therefore, the first motivation of the present study is to explore bedload processes across the wave breaking zone.

Research has further revealed that transport in the breaking region is size-selective, i.e. differs for each grain size class within a sediment sample. Observations of graded sediment transport under oscillatory sheet flow conditions have shown that coarser grains are transported more easily than finer particles because they are more exposed (de Meijer et al., 2002; Hassan and Ribberink, 2005). The suspended load transport generally contains a relatively high fraction of fine-grained particles which are more easily entrained and mixed than coarse grains (Nielsen, 1992; Wiberg et al., 1994; Davies and Thorne, 2016) and which are advected by the mean current (Sistermans, 2002). In time, the removal of fine-grained particles from the bed may lead to coarsening of the seabed. This may even lead to the formation of erosion-resistant bed surface layers of coarse grains ('armouring'), which can significantly reduce sediment pick-up and transport rates (Nielsen, 1992; Wiberg et al., 1994). Finn et al. (2016) suggest, based on detailed simulations with a particle-based numerical model, that for sheet flow conditions such armour layers may already develop after one wave cycle.

Grain size observations in the field have revealed a shoreward coarsening of the sand bed due to size-selective transport mechanisms (Murray, 1967; Richmond and Sallenger, 1984). Observations in the field (Wang et al., 1998) and laboratory (Koomans, 2000; Srisuwan et al., 2015; Broekema et al., 2016) have further revealed a relatively large fraction of coarse grains on breaker bar crests, while bar troughs are composed of relatively fine sediment. The transport of graded particles can be modeled by calculating transport for different grain classes independently (e.g. Reniers et al., 2013), with the optional inclusion of a 'hiding/exposure' factor that accounts for reduced or enhanced exposure of certain grain classes (e.g. van Rijn, 2007). The inclusion of size-selective transport can significantly alter numerical predictions of breaker bar position and shape compared to simulations with uniform sand (Van Rijn, 1998; Srisuwan and Work, 2015). This illustrates the relevance of grain sorting processes for the understanding and modeling of breaker bar morphodynamics; yet no study has examined the temporal evolution of a breaker bar's grain composition in relation to measured suspended and bedload transport rates. This forms the second motivation of the present study.

This study presents high-resolution measurements of sand transport processes under a large-scale laboratory plunging wave and along a fully mobile medium-sand breaker bar. Data from the same experiment were used before to study wave breaking effects on wave bottom boundary layer hydrodynamics (van der Zanden et al., 2016) and on suspension processes (van der Zanden et al., 2017). The present study particularly addresses four matters: (i) the potential effects of wave breaking on sheet flow dynamics, which are measured using a novel conductivity-based concentration measurement system (CCM^{+}); (ii) the cross-shore variation in bedload transport rates in relation to the hydrodynamic forcing and to the suspended transport; (iii) the contributions of net bedload and suspended sand transport to the morphological evolution of the breaker bar; (iv) grain size sorting of suspended sediment and of the sand bed.

The paper is organized as follows. Section 2 explains the instrument set-up and data treatment steps. Section 3 presents the measured bed evolution and the main flow parameters in the experiment. Sheet flow observations and estimated bedload transport rates are presented in Section 4. Section 5 presents and discusses the cross-shore-varying contributions of suspended and bedload transport to breaker bar morphodynamics. Section 6 presents measurements of grain sorting in suspended sediment profiles and along the cross-shore bed profile. Results are discussed in Section 7; Section 8 presents the main conclusions.

2. Experimental description

2.1. Facility and test conditions

The experiments were conducted in the large-scale CIEM wave flume at the Universitat Politècnica de Catalunya (UPC) in Barcelona. The flume is 100 m long, 3 m wide and 4.5 m deep, and is equipped with a wedge-type wave paddle. Fig. 1 shows the experimental set-up and bed profile for the present study. Cross-shore coordinate x is defined positively towards the beach, with $x = 0$ at the toe of the wave paddle. Vertical coordinate z is defined positively upwards with $z = 0$ at the still water level (SWL). ζ is used for vertical coordinate positive upwards from the local bed level.

The bed profile consisted of medium-grained sand of which the sediment characteristics are detailed in Section 2.4. The reference bed profile consisted of a bar-trough configuration (Fig. 1a, black line) that is roughly divided into an offshore slope of the breaker bar (x = 35.0–54.8 m; steepness $\tan(\alpha) = 0.10$), followed by a steeper shoreward-facing bar slope (x = 54.8–57.5 m; $-\tan(\alpha) = 0.21$), and a mildly sloping bed shoreward from the bar trough (x = 57.5–68.0 m; $\tan(\alpha) = 0.01$). The profile shoreward of the mobile test section ($x > 68.0$ m) followed a slope $\tan(\alpha) = 0.13$, was fixed with geotextile, and was covered with permeable

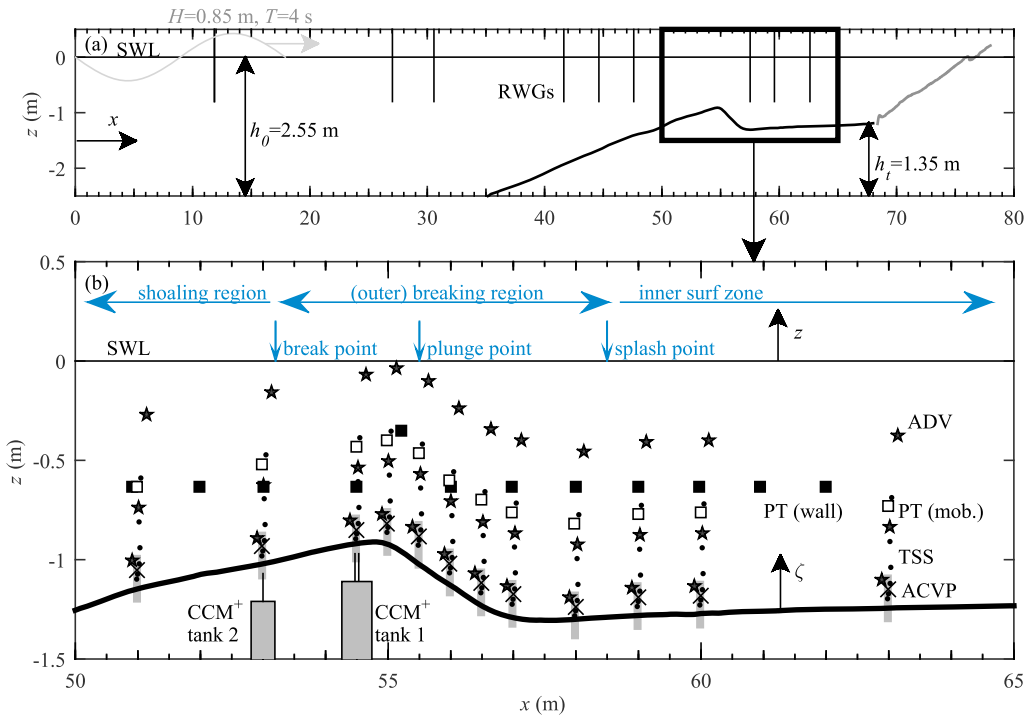

Fig. 1. Experimental set-up and measurement locations. (a) Reference bed profile (black line) and fixed beach (grey line), plus locations of resistive wave gauges (RWGs, vertical black lines); (b) Measurement positions of ADVs (star symbols), mobile-frame Pressure Transducers (PT, white squares), wall-deployed PTs (black squares), Transverse Suction System nozzles (TSS, black dots), Optical Backscatter Sensor (black crosses), measuring windows of mobile-frame Acoustic Concentration and Velocity Profiler (ACVP, grey rectangles) and locations of the two CCM$^+$ tanks.

concrete slabs to promote wave energy dissipation. In this bed configuration, the breaker bar and trough were deliberately separated from the fixed beach to ensure that the inner surf and swash zone processes over the sloping beach did not affect the hydrodynamic and sand transport processes in the bar-trough region.

The experiments involved monochromatic waves with wave period $T = 4.0$ s and wave height $H_0 = 0.85$ m at water depth $h_0 = 2.55$ m near the wave paddle. Table 1 presents an overview of dimensionless parameters that characterize the wave and beach conditions (c.f. Dean and Dalrymple, 2001). The wave conditions correspond to a surf similarity parameter $\xi_0 = 0.54$ and, matching the classification of Battjes (1974), resulted in plunging breaking waves. The equilibrium beach state (barred or non-barred) can be predicted based on a combination of parameters. Several indicators for barred profiles have been suggested, i.e. $H_0/L_0 > 5.5\pi w_s/(gT)$ (Kriebel et al., 1986; Dean and Dalrymple, 2001), $H_0/L_0 < 0.0007\Omega^3$ (Kraus and Larson, 1988), and $Pr > 1.0{\cdot}10^4$ (Dalrymple, 1992). Based on each of these three indicators, the present morphodynamic experiment is expected to produce a barred bed profile (c.f. Table 1).

Following Svendsen et al. (1978), we define the 'break point' as the location where the wave starts to overturn (at $x = 53.0$ m). The 'plunge point' ($x = 55.5$ m) is the location where the plunging jet strikes the water surface (Peregrine, 1983). The 'splash point' ($x = 58.5$ m) is the location where the water mass pushed up by the plunging jet strikes the water surface a second time, and where a surf bore starts to develop (Smith and Kraus, 1991). These regions are used to define the shoaling zone (up to break point; $x \leq 53.0$ m), the breaking region (between break and splash points; $53.0 < x < 58.5$ m) and the inner surf zone (shoreward from splash point; $x > 58.5$ m) following Svendsen et al. (1978). In Fig. 1b these points and regions are included for reference.

Table 1
Overview of dimensionless parameters that characterize the wave and beach profile conditions. H_0 and L_0 are the deep-water wave height and wave length, respectively, $\tan(\alpha)$ is the offshore bar slope, $w_s = 0.034$ m/s is the sand fall velocity, and g is the gravitational acceleration.

Parameter	Definition	Value
Deep water wave steepness	H_0/L_0	0.034
Surf similarity parameter (Battjes, 1974)	$\xi_0 = tan(\alpha)/\sqrt{H_0/L_0}$	0.54
Dean number (Dean, 1973)	$\Omega = H_0/w_sT$	6.3
Fall velocity parameter (Dean, 1973)	$\pi w_s/(gT)$	0.0027
Profile parameter (Dalrymple, 1992)	$Pr = gH_0^2/(Tw_s^3)$	$4.5{\cdot}10^4$
Fall velocity Froude number (Dalrymple, 1992)	$F_w = w_s/\sqrt{gH_0}$	0.20

2.2. Instrumentation

Near-bed and outer-flow hydrodynamics and suspended sediment concentrations were measured with a vertical array of acoustic instruments deployed from a custom-built mobile frame (Fig. 2). This frame consisted of stainless-steel tubing with 30 mm diameter and was designed such that it would have minimum flow perturbation while being sufficiently stiff to withstand wave impact. The frame was mounted to a horizontally-mobile trolley on top of the flume, and could be vertically positioned with sub-mm accuracy using a spindle. The mobile frame set-up enabled measurements at various cross-shore positions, while maintaining an approximately equal elevation of the instrument array with respect to the bed at the start of each run.

The velocity was measured at outer-flow elevations using three acoustic Doppler velocimeters (ADVs) and near the bed with an acoustic concentration and velocity profiler (ACVP), all deployed from the mobile frame. The ACVP is a pulse-coherent acoustic Doppler system for measuring co-located particle velocity and sand concentration (Hurther et al., 2011). In the present experiment, the ACVP operated at an acoustic frequency of 1 MHz and measured the two-component (u, w) particle velocity and sand concentration over a 10–15 cm vertical profile directly above the bed with 1.5 cm vertical bin resolution and 70 Hz sampling frequency. Sand concentrations were obtained by inverting the reflected ACVP-measured acoustic intensity signal using calibration measurements by a six-nozzle Transverse Suction System (TSS) and an optical backscatter sensor (OBS). The ACVP directly measured the instantaneous

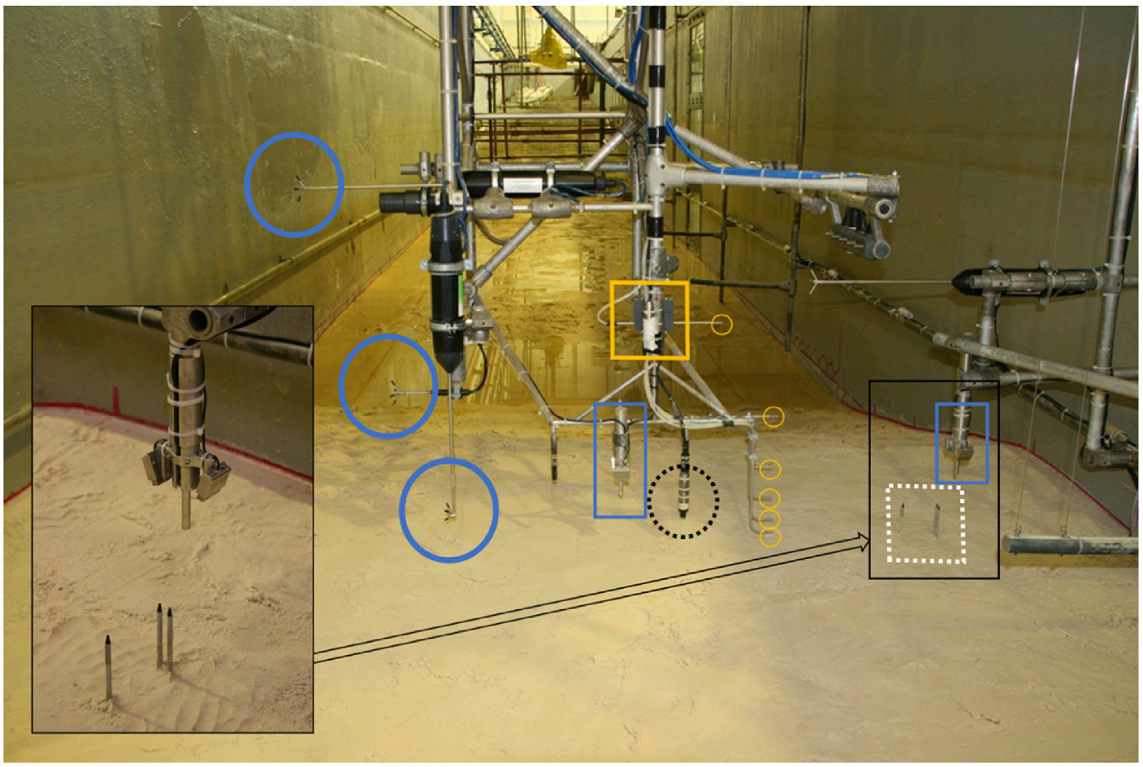

Fig. 2. Mobile measuring frame and instrumentation. Instrumentation includes three acoustic Doppler velocimeters (ADVs, blue solid circles), one pressure transducer (PT, yellow square), a six-nozzle transverse suction system (TSS, yellow circles), an optical backscatter sensor (dashed circle) and an acoustic concentration and velocity profiler (ACVP, blue rectangle). Inset shows close-up of CCM$^+$ tank 1 sensors (dashed square) and another ACVP, deployed from the sidewall. Note that the CCM$^+$ sensors are raised here above the bed; during the experiment the tops of the sensors are within ±1 cm from the bed. (For interpretation of the references to colour in this figure legend, the reader is referred to the web version of this article.)

horizontal sand flux $\phi_x = uC$, which for the present experiment could be obtained at a measurement frequency of 5 Hz after removal of acoustic Doppler noise contaminations. More details on the velocity, suspended sand concentration, and suspended sand flux measurements can be found in van der Zanden et al. (2016, 2017).

Time-varying sediment concentrations in the sheet flow layer were measured using two Conductivity-based Concentration Measurement (CCM$^+$) tanks (Fig. 1b). These tanks were located at the bar crest at $x = 53.0$ m (at break point where wave starts to overturn) and at $x = 54.5$ m (between break point and plunge point). For the high sand concentrations (100–1600 kg/m^3) in the sheet flow layer, the measured conductivity of a water-sand mixture is a linear function of sand concentration, which makes the conductivity-based measuring principle highly suitable for studying sheet flow dynamics (Ribberink and Al-Salem, 1995; Dohmen-Janssen and Hanes, 2002; Lanckriet et al., 2013). The CCM$^+$ tanks in the present study are equipped with one single conductivity probe plus a combined double probe (for tank 1), or with one single probe (tank 2), and sample with a 1000 Hz data rate. The two sensors of the combined probe of tank 1 (Fig. 2 inset) are spaced 1.5 cm in cross-shore direction and can be used to estimate particle velocities in the sheet flow layer by cross-correlating both sensors' signals (see McLean et al., 2001). The probes penetrate the sheet flow layer from below to minimize flow disturbance.

The tanks are equipped with a bed level tracking system that enables automatic repositioning of the probes with sub-mm accuracy and which is fully described in van der Zanden et al. (2015a). In tracking mode, the probes track the continuous elevation of the bed-water interface, hence they measure the bed evolution at wave-averaged or longer time scales. Alternatively, the user can select to use the probes to measure sheet flow concentrations at a fixed absolute elevation (i.e. no tracking). In the present study, both types of measurements were alternated for fixed intervals of 60 s: sheet flow concentration measurements were obtained at elevations of −2, +0, and +4 mm with respect to the bed; after each of these intervals, the probes were repositioned to the local bed level by activating the tracking system. Through this procedure, concentrations were sampled over the complete sheet flow layer while at the same time the bed level was measured with ±1 mm accuracy.

A six-nozzle Transverse Suction System (TSS) was used to collect samples of suspended sediment at $\zeta \approx 0.02$, 0.04, 0.10, 0.18, 0.31 and 0.53 m (see van der Zanden et al., 2017, for more details). The collected samples were dry-weighed and packed. The grain size characteristics were determined at the University of Aberdeen using a Beckman Coulter LS 13 320 laser diffraction particle sizer (specifications found in the user manual: Beckman Coulter Inc, 2008). Previous experience using this particle sizer indicated a minimum amount of 2.5 g sand (corresponding to obscuration > 5%) to be required for a reliable estimate of the size distribution. This minimum amount was reached for all TSS samples, except for some of the samples obtained at the furthest offshore location ($x = 51.0$ m) or at elevations above wave trough level. For these combinations of locations/nozzles, samples of different runs but for the same nozzle and cross-shore location were combined to obtain the required amount of sand.

Water surface elevation was measured with a combination of resistive wave gauges (RWGs) in the shoaling zone and pressure transducers (PTs) in the breaking and inner surf zone. Bed profile measurements were obtained at 2 cm cross-shore resolution along two transects, at lateral distances of 0.1 and 0.7 m at either side of the flume's centerline, using echo sounders deployed from a second mobile trolley. The echo sounders had an estimated accuracy of ±1 cm and the mean of both sensors is used to study the bed profile evolution and net sediment transport rates.

2.3. Measurement procedure

One experiment consisted of 90 min of waves, divided over six 15-min runs, during which the bed profile evolved. The bed profile was measured prior to the first run and after every 2nd run, i.e. at $t = 0$, 30, 60

and 90 min. After the sixth run, the flume was drained. The reference bed profile, drawn as template on the flume wall, was then restored by shoveling back the transported sand and flattening any bed forms that were generated. Each experiment was repeated 12 times, with the mobile measuring frame positioned at a new location for each experiment. The bed profile evolution and hydrodynamics were very similar for each experiment (van der Zanden et al., 2016) and the adopted procedure resulted in a high spatial coverage of velocity and concentration measurements (Fig. 1b).

Sediment samples of the bed were taken at 12 cross-shore locations at the start of the campaign (corresponding to horizontal test section), after the initial start-up stage (corresponding to reference bed level and $t = 0$ min) and at the end of the final experimental repeat ($t = 90$ min). Bed samples were taken at each cross-shore location by carefully scraping off the upper 1–2 cm of the sand bed at three positions separated in cross-flume direction. In the inner surf zone, where bed forms occurred, the samples were taken over a complete ripple length. When restoring the profile, the sediment was reshuffled by bringing sediment from the shoaling to the inner surf zone and vice versa.

2.4. Sediment characteristics

Fig. 3 shows the cumulative grain-size distribution measured with the laser-diffraction particle sizer for one of the bed samples at the start of the campaign. The accordingly obtained median sediment diameter (D_{50}) is 0.29 mm. This is somewhat higher than values of 0.25 mm found for the exact same sediment by independent sieving tests at the CIEM lab and by sieving tests by the sediment supplier. This difference is explained by sand grains not being perfect spheres: the particle sizer measures an equivalent 'perfect sphere' diameter; sieving yields the diameter of the smallest cross-sectional area of a non-spherical grain (Eshel et al., 2004). The degree of uniformity is quantified through the geometric method of moments σ_g (Blott and Pye, 2001). With a measured $\sigma_g = 1.36$, the sand is classified 'well sorted' following Blott and Pye (2001). The sand grains had a measured mean settling velocity $w_s = 0.034$ m/s.

2.5. Data treatment

Data treatment steps related to hydrodynamics and suspended sediment concentrations and fluxes is described extensively in van der Zanden et al. (2016, 2017). These steps are only briefly repeated here.

Visual observations and measurements revealed that a hydrodynamic equilibrium established for each run after approximately 5 min. Therefore, only the last 10 min of data from each run (corresponding to about 150 wave cycles) were used for analysis. Flume seiching induced a standing wave with an approximately 45-s period. The seiching wave could be identified in auto-spectra of water surface and horizontal velocities, but not in bed level and suspended sediment concentrations. Hence, its effect on sediment processes is considered negligible. The standing wave was removed from water surface and velocity time series by applying a high-pass filter with a cut-off frequency of 0.125 Hz (half the primary-wave frequency).

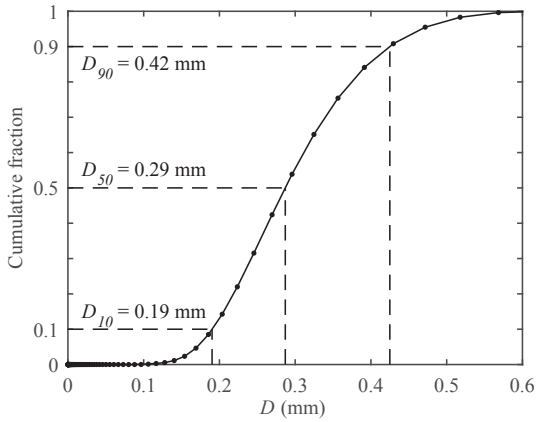

Fig. 3. Cumulative grain-size distribution of bed sediment at the start of the experiment (obtained by the laser-diffraction particle sizer).

The phase-averaged value of a variable ψ are annotated with angle brackets and are calculated over N wave repetitions as

$$\langle\psi\rangle(t) = \frac{1}{N}\sum_{n=1}^{N}\psi(t+(n-1)T). \tag{1}$$

Reference zero-up crossings, required to phase-reference each wave cycle prior to phase-averaging, were based on water surface measurements at $x = 47.6$ m. Data were phase-referenced such that $t/T = 0$ corresponds to maximum surface elevation (wave crest) at the beginning of the test section ($x = 50.0$ m). Phase-averaged horizontal velocities $\langle u\rangle$ consist of a time-averaged component $\bar{u}$, i.e.

$$\bar{u} = \frac{1}{T}\int_0^T \langle u(t)\rangle dt, \tag{2}$$

and a periodic component $\tilde{u} = \langle u\rangle - \bar{u}$. Root-mean-squared $\tilde{u}$ is denoted $\tilde{u}_{rms}$. The turbulent velocity components u', v', w' were obtained through a Reynolds decomposition based on the phase-average, i.e. $u' = u - \langle u\rangle$, and were subsequently used to calculate the phase- and time-averaged turbulent kinetic energy (TKE). Note that following this definition for u', the phase-coherent motion of the plunging jet is part of the period component $\tilde{u}$ and does not contribute to TKE. More details on turbulence data processing are given by van der Zanden et al. (2016).

The CCM$^+$ tanks were positioned at fixed cross-shore locations during the experiment. Measurements were phase-averaged for each 15-min stage of bar development over all 12 experimental repeats, resulting in a large number of wave repetitions ($N > 1000$). For the time-varying sheet flow concentration measurements $C(\zeta, t)$, $\zeta = 0$ is defined as the bed level during the zero-down crossing of the wave when the bed is considered to be at rest ('immobile bed level'). Intra-wave bed level fluctuations are preserved in phase-averaged results. $C(\zeta, t)$ measurements were bin-averaged, where the bin class was based on the relative elevation ζ and the bin resolution $\Delta\zeta = 0.25$ mm. For each wave phase and elevation bin, $\langle C(\zeta_i, t)\rangle$ is calculated as the median of concentration measurements in the range $\zeta_i - \Delta\zeta/2 < \zeta_i < \zeta_i + \Delta\zeta/2$.

For calculating sand particle velocities in the sheet flow layer, the concentration time series of the two sensors of the combined probe were first high-pass filtered ($f_{cutoff} = 1$ Hz). The cross-correlation of the two sensors' signals was calculated over regular time intervals $\Delta t = 0.1$ s. Each wave cycle was assigned a concentration bin class (bin resolution $\Delta C = 0.1$ m^3/m^3) based on wave-averaged concentration. The cross-correlation output was then averaged for each ΔC bin class and each wave phase $\Delta t/T$. The bin-averaged cross-correlation is used to quantify the time lag between both signals, which with known distance between the sensors is translated into a particle velocity (see further McLean et al., 2001; van der Zanden et al., 2015a).

Volumetric total sediment transport rates q_{tot}, due to contributions by both bedload and suspended load, can be obtained from measured bed profile measurements z_{bed} by solving the Exner equation:

$$q_{tot}(x) = q_{tot}(x-\Delta x) + \Delta x(1-\varepsilon_0)\frac{\Delta z_{bed}(x)}{\Delta t}. \tag{3}$$

Here, ε_0 is the sand porosity (0.4 if loosely packed), Δx is the horizontal resolution of z_{bed} measurements (=0.02 m) and Δt is the time interval between two consecutive profile measurements (30 min). Eq. (3) can be solved if q_{tot} is known at one x location. With $q_{tot} = 0$ at the left-hand (i.e. $x = 35$ m) and right-hand boundary ($x = 68$ m) of the mobile test section, q_{tot} can be solved iteratively by starting from either the left- or the right-hand side of the profile. This yields two estimates of q_{tot}, annotated q_{lhs} and q_{rhs} respectively. The estimates q_{lhs} and q_{rhs} are likely

different due to variations in the horizontally-integrated volume of the two profile measurements used to quantify Δz_{bed}. These variations can be attributed to sampling errors of the acoustic sensors, 3D bed forms, variations in packing density and porosity, and non-uniformity of the bed profile (e.g. Baldock et al., 2011). For the present experiment, the cross-shore-integrated measured bed profile increased on average by 0.22 m^2 between the start and end of the experiment, which is equivalent to a mean overestimation of $\Delta z_{bed}(x)$ by 0.007 m at the end of the experiment. This increase can be attributed to scouring that occurred near the flume side-walls and which resulted in sand accumulation around the centerline of the wave flume, where the profile was measured.

Although the systematic error of 0.007 m in Δz_{bed} is considered small compared to the main bed level changes during the experiment (Δz_{bed} of $O(0.1$ m)), it leads to a significant cumulative error in $q_{tot}(x)$ (up to $2{\cdot}10^{-5}$ m^2/s). Depending on distance to each horizontal boundary of the test section, q_{lhs} or q_{rhs} is more accurate. The error in the volumetric total transport rate q_{tot} can therefore be minimized by calculating the weighted average of both estimates:

$$q_{tot}(x) = \left(\frac{x_{end} - x}{x_{end} - x_0}\right) q_{lhs}(x) + \left(\frac{x - x_0}{x_{end} - x_0}\right) q_{rhs}(x), \quad (4)$$

with $x_0 = 35$ m and $x_{end} = 68$ m being the left- and right-hand boundary of the mobile bed profile, respectively. The transport rate $q_{tot}(x)$ was calculated for each experimental repeat using Eqs. (3) and (4), and was then averaged over all repeats. The resulting estimated error in q_{tot} varies between 0 and $1{\cdot}10^{-5}$ m^2/s, with smallest values at the left- and right-hand boundaries and highest values for the middle of the test section.

3. Hydrodynamics and bed profile evolution

This section presents an overview of the main hydrodynamics and the bed profile evolution. The reader is referred to van der Zanden et al. (2016) for a more detailed description of the near-bed hydrodynamics (including turbulence) in the present experiment and to van der A et al. (2017) for an extensive analysis of the outer-flow hydrodynamics for an accompanying rigid-bed experiment with the same bed profile and wave conditions.

3.1. Hydrodynamics

Table 2 presents an overview of the main hydrodynamic parameters at the 12 measurement locations. Fig. 4a shows the wave crest and trough levels and the time-averaged water level $\bar{\eta}$. The wave height ($H = \eta_{crest} - \eta_{trough}$) reduces by 50% between the break point (around $x = 53.0$ m) and splash point ($x = 58.5$ m). Water levels $\bar{\eta}$ show a set-down at the shoaling locations and set-up at the inner surf zone. Fig. 4b shows time-averaged velocity $\bar{u}$ and maximum onshore and offshore horizontal velocity $\langle u \rangle_{max}$ and $\langle u \rangle_{min}$. These values are measured at the wave bottom boundary layer (WBL) overshoot elevation δ ($\zeta \approx 0.02$ m) and are averaged over the complete experiment ($t = 0$–90 min, i.e. over six runs). Along the offshore slope up to the bar crest ($x = 51.0$–55.0 m), $\langle u \rangle_{max}$ and $\langle u \rangle_{min}$ remain roughly constant. Time-averaged velocity magnitudes are lowest at $x = 51.0$ m and increase towards the bar crest. The skewness and asymmetry of $\tilde{u}$ (Table 2) show that the intra-wave shape of $\tilde{u}$ changes significantly along the offshore slope. Most notable is the large asymmetry at $x = 53.0$ m at the onset of breaking-wave overturning. Along the shoreward-facing bar slope ($x = 55.5$–58.0 m), the combination of decreasing H and increasing h leads to a substantial decrease in orbital velocity amplitude while at the same time the magnitudes of offshore-directed time-averaged velocity $\bar{u}$ (undertow) increases. Undertow velocity magnitudes decrease again in the inner surf zone ($x > 58.5$ m).

Fig. 4c shows the time-averaged TKE ($\overline{k}$) at outer-flow elevation and close to the bed. The latter, k_b, is defined here as the maximum $\overline{k}$ measured inside the WBL. Turbulence production by wave breaking leads to large magnitudes of outer-flow $\overline{k}$ near the plunge point at $x = 55.5$ m $\overline{k}$ decreases towards the bed at most locations, which indicates that wave breaking is the primary source of turbulence. Breaking-generated turbulence is advected to offshore locations while gradually dissipating, and consequently, $\overline{k}$ decreases from the breaking zone in offshore direction (from $x = 55.5$ to 51.0 m). Turbulent kinetic energy inside the WBL (k_b) follows a similar cross-shore pattern as outer-flow $\overline{k}$, i.e. it increases by an order of magnitude between the shoaling zone at $x = 51.0$ m to the breaking region at $x = 56.0$ m. This increase occurs in spite of a decrease in $\langle u \rangle_{max}$ and $\langle u \rangle_{min}$, which suggests that the increase in k_b is due to the invasion of breaking-generated turbulence into the WBL. Further shoreward, k_b decreases above the bar trough (around $x = 58.0$ m) and increases gradually throughout the inner surf zone ($x > 58.5$ m) due to the presence of sand ripples.

Flow disturbance by the mobile frame contributed locally to the measured TKE. The contributions of frame-generated turbulence to TKE were assessed by inter-comparing velocity measurements that were collocated at x, z coordinates but positioned at different cross-flume distances from the frame (van der A et al., 2017). Notable contributions of frame-generated turbulence to ADV-measured TKE appeared only at locations where other sources of turbulence (bed friction and wave breaking) were small: at $x = 51.0$ m (shoaling zone) and $x > 60.0$ m (inner surf zone).

3.2. Bed profile evolution and net total transport

Fig. 4a shows the bed profile evolution. The bar crest grows and

Table 2
Hydrodynamic and bed parameters at each measurement location: water depths (h); wave heights (H); ADV-measured velocity statistics at $\zeta = 0.11$ m, with maximum onshore and offshore phase-averaged horizontal velocity, semi-excursion length ($a = \sqrt{2}T\tilde{u}_{rms}/2\pi$), velocity skewness ($Sk(u) = \overline{\tilde{u}^3}/\tilde{u}^3_{rms}$), velocity asymmetry ($Asy(u) = -\mathrm{H}(\overline{\tilde{u}})^3/\tilde{u}^3_{rms}$, where H marks Hilbert transform (e.g. Elgar, 1987), local bed slope $\tan(\alpha) = dz_{bed}/dx$ at the start ($t = 0$ min) and end ($t = 90$ min) of the experiment. The listed hydrodynamic parameters were measured during the first run of each experimental repeat ($t = 0$–15 min).

x (m)	h (m)	H (m)	$\bar{u}$ (m/s)	$\langle u \rangle_{max}$ (m/s)	$\langle u \rangle_{min}$ (m/s)	a (m)	$Sk(u)$	$Asy(u)$	$\tan(\alpha)$, $t = 0$ min	$\tan(\alpha)$, $t = 90$ min
51.0	1.10	0.79	−0.13	1.04	−0.83	0.54	0.61	0.68	0.08	0.12
53.0	0.97	0.74	−0.22	0.80	−0.94	0.48	0.44	1.01	0.06	0.12
54.5	0.88	0.64	−0.19	0.84	−0.85	0.47	0.50	0.82	0.04	0.06
55.0	0.88	0.60	−0.24	0.78	−0.90	0.47	0.48	0.76	−0.10	0.03
55.5	0.97	0.51	−0.23	0.57	−0.83	0.39	0.36	0.75	−0.22	−0.12
56.0	1.10	0.50	−0.30	0.25	−0.82	0.31	0.06	0.77	−0.20	−0.45
56.5	1.19	0.53	−0.51	0.05	−0.83	0.25	0.67	0.76	−0.18	−0.51
57.0	1.24	0.48	−0.54	0.02	−0.78	0.23	0.95	0.58	−0.08	−0.35
58.0	1.28	0.47	−0.46	0.01	−0.71	0.21	0.82	0.79	0.02	0.11
59.0	1.28	0.43	−0.36	0.13	−0.71	0.23	0.39	0.88	0.02	0.16
60.0	1.26	0.42	−0.36	0.17	−0.66	0.24	0.67	0.68	0.03	0.02
63.0	1.26	0.41	−0.34	0.19	−0.58	0.23	0.79	0.45	0.01	0.01

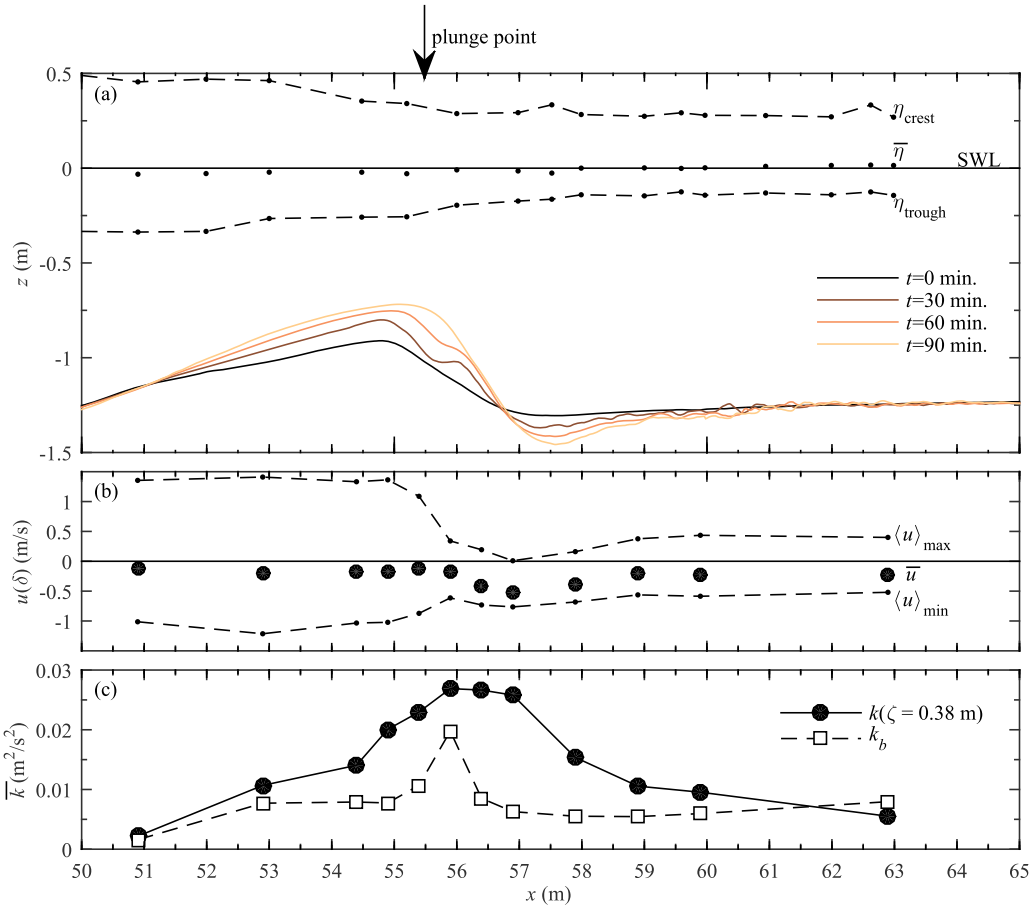

Fig. 4. (a) Bed profile evolution (solid lines, with each line representing the mean value over all experimental days), and water levels for t = 0–15 min (dots and dashed lines depict time-averaged and envelope, respectively); (b) ACVP-measured horizontal velocity at the WBL overshoot elevation $\zeta = \delta$, for t = 0–90 min, time-averaged (circles) and maximum phase-averaged onshore and offshore velocity (dots and dashed line); (c) Time-averaged turbulent kinetic energy over the experiment (t = 0–90 min) at outer-flow elevation ζ = 0.38 m (measured with ADV, solid line + circles) and inside the WBL (measured with ACVP, dashed line + squares).

migrates slightly onshore during the experiment. This leads to an increase in the bar's offshore slope from tan(α) = 0.10 to 0.13 and an increase in the surf similarity parameter ξ_0 from 0.54 to 0.68. At the same time the bar trough deepens, resulting in a steepening of the shoreward slope of the breaker bar from tan(α) = −0.21 to −0.47. At t = 90 min, this slope approaches the natural angle of repose (tan(α) ≈ 0.5 to 0.7) for sandy materials (Nielsen, 1992). Table 2 includes the local bed slope at the start and end of the experiment for each measurement location.

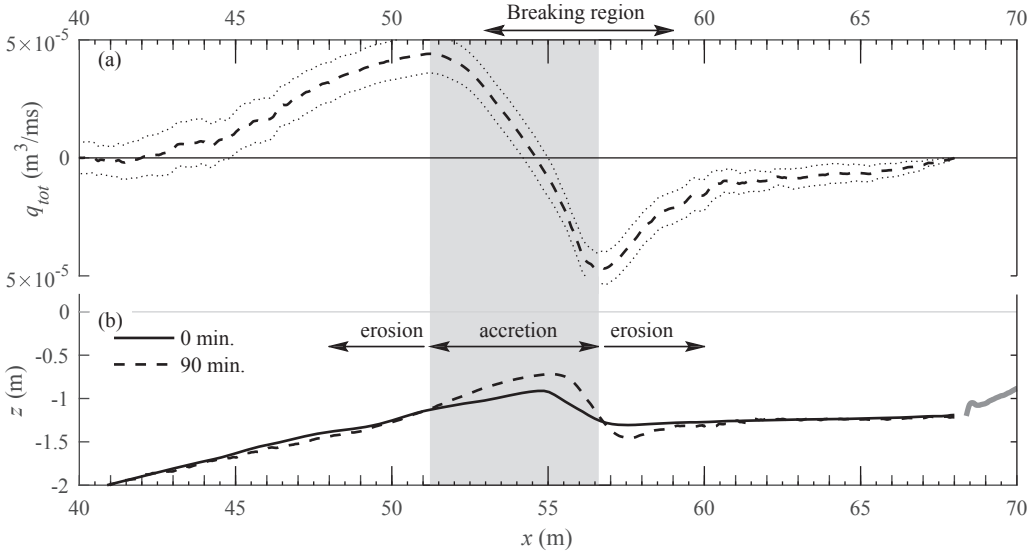

Fig. 5. (a) Total transport during the experiment (t = 0–90 min) obtained through Eq. (4), mean values (dashed) ±95% confidence interval (dotted) over all experimental repeats; (b) Initial (solid) and final (dashed) bed profile. The grey shading marks the region of net accretion.

Bed forms were observed after draining the flume. The bed was flat in the shoaling region and at the bar crest (x = 48.0–55.5 m), indicating bedload transport in the sheet flow regime. Quasi-2D bed forms (quasi-uniform in cross-flume direction) were identified along the shoreward slope of the bar (x = 55.5–57.0 m), where they migrated progressively offshore. These bed forms were asymmetrically shaped, with a relatively steep offshore slope and a mild shoreward slope. Shoreward-facing lunate-shaped bed forms were formed at the bar trough (x = 57.0–59.0 m). At the inner surf zone a gradual transition to quasi-2D bed features occurs (from x = 59.0–62.0 m). Further shoreward these features became increasingly irregular while their wave length reduced, resulting in 3D sand ripples (x = 62.0 m–68.0 m). In the inner surf zone (x > 58.5 m) bed form lengths were of similar magnitude as the orbital semi-excursion length a. The bed forms in the breaking region had lengths that exceed a by a factor 2 to 5.

The bar growth can be explained by accumulation of primarily onshore-directed total transport at shoaling locations and offshore-directed transport in the breaking and inner surf zone (Fig. 5). The reversal of transport direction occurs near the breaker bar crest (x = 54.5 m), about 1 m offshore from the plunge point. The sharp gradients dq_{tot}/dx at the breaking region indicate strong cross-shore non-uniformity in sand transport processes. Note that q_{tot} is not constant throughout the experiment; instead, the magnitudes of onshore and offshore q_{tot} decrease as the breaker bar evolves towards a semi-equilibrium state (van der Zanden et al., 2015b). This morphologic feedback of profile evolution on time-evolving transport rates is not further considered in the present study.

4. Bedload transport processes

This section first presents and discusses sheet flow measurements (Sections 4.1–4.3) which are compared with oscillatory sheet flow observations in tunnels and under non-breaking waves to assess the effects of wave breaking. Next, Section 4.4 presents the cross-shore-varying bedload transport rates and relates these to the near-bed hydrodynamics.

4.1. Sheet flow layer concentrations

The sheet flow layer behavior is explored using CCM$^+$ measurements at two locations near the breaker bar crest, i.e. at x = 53.0 m (below break point) and x = 54.5 m (between break point and plunge point). Fig. 6c,d shows phase-averaged concentrations $<C(\zeta, t)>$, bin-averaged for vertical elevations ζ with bin resolution $\Delta\zeta$ = 0.25 mm and based on a minimum of three wave repetitions. Due to the chosen settings for probe repositioning during acquisition, this minimum was not obtained for each ζ bin class (which explains the data gaps e.g. at $\zeta \approx 2$ mm, Fig. 6c). Fig. 6e,f also shows concentration time series, but for these panels C was phase-averaged for seven bins based on the wave-averaged concentration for each wave cycle. The latter data representation preserves the temporal variation in C that occurs at intra-wave time scale and it has been adopted throughout many sheet flow studies (Ribberink and Al-Salem, 1994; O'Donoghue and Wright, 2004; Schretlen, 2012). This approach is especially useful to study phase lags between the upper sheet flow layer (region above the 'immobile bed level', i.e. ζ > 0, with typical concentrations lower than 0.3 m^3/m^3) and the erosion layer (ζ < 0, C > 0.3 m^3/m^3).

Despite sheet flow layers being rather thin, of O(mm), the CCM$^+$ manages to resolve the time-varying concentrations adequately. This is partly ascribed to the new automatic probe repositioning system, which allows measurements of the time-varying relative bed level with higher accuracy than previous versions of the CCM system. At both CCM$^+$

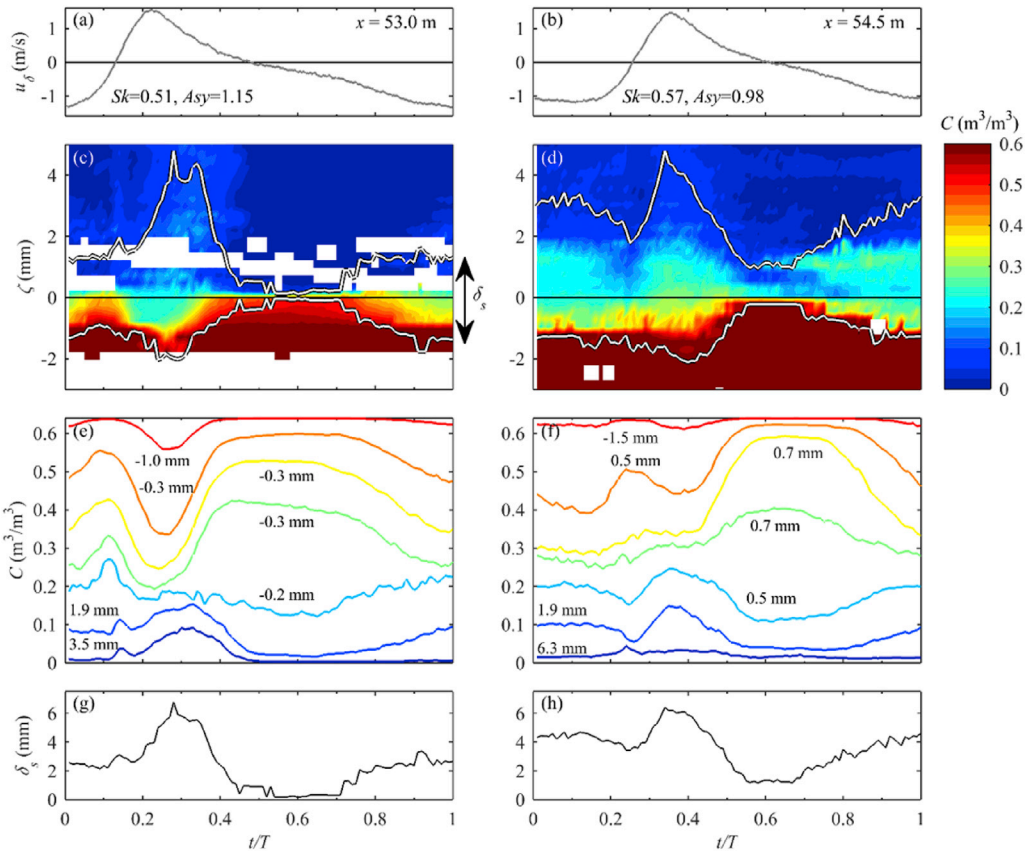

Fig. 6. Time series of phase-averaged CCM$^+$ measurements at x = 53.0 m (left) and x = 54.5 m (right), for final stage of bar development (t = 75–90 min). (a,b) ACVP-measured velocities at $\zeta = \delta$, including non-dimensional velocity skewness (Sk) and acceleration skewness (Asy) values. (c,d) Concentration contour, with white lines marking the erosion depth and the top of the sheet-flow layer; (e,f) Concentration time series, phase-averaged for 7 wave-averaged concentration bins. For each concentration bin, the calculated relative position ζ (standard deviation ±1 mm) is indicated in the panels; (g,h) Sheet flow layer thickness.

locations, instances of peak offshore and onshore velocities lead to a quasi-instantaneous concentration decrease in the erosion layer ($C < 0.3$ m^3/m^3) and a simultaneous increase in the upper sheet flow layer ($C < 0.3$ m^3/m^3). The erosion layer responds layer by layer to velocity forcing, i.e. concentrations at elevations deeper in the erosion layer ($\zeta \approx -2$ to -1 mm) respond slightly later than concentrations near $\zeta = 0$. Hence, no evidence of a rapid pressure-induced mobilization of a complete 'block' of sediment ('plug flow', c.f. Sleath, 1999) is found. The short increase in upper sheet flow layer sediment concentration around flow reversal ($t/T = 0.17$) at $x = 53.0$ m has also been observed in oscillatory sheet flow conditions and may relate to shear instabilities around flow reversal (Ribberink and Al-Salem, 1995; O'Donoghue and Wright, 2004).

4.2. Sheet flow layer thickness

The time-varying sheet flow layer δ_s is the difference between the intra-wave time-varying bottom (i.e. erosion depth) and the top of the sheet flow layer (i.e. the elevation with $\langle C \rangle = 0.08$ m^3/m^3; Dohmen-Janssen and Hanes, 2002). These elevations were established by fitting the empirical function of O'Donoghue and Wright (2004) for vertical sheet flow concentration profiles through the time-varying concentration measurements (the approach is described more extensively in van der Zanden et al., 2015a). The function fitted well through the measurements ($r^2 > 0.9$ for each profile). Fig. 6c,d includes the time-varying erosion depth and top of the sheet flow layer and Fig. 6g,h shows the intra-wave sheet flow thickness δ_s.

The sheet flow thickness shows similar phase behavior as the near-bed velocity magnitude, which again illustrates the quasi-instantaneous response of sheet flow pick-up to near-bed velocity. At $x = 53.0$ m, δ_s returns to near zero during the crest-to-trough flow reversal, which indicates that most of the sediment that was entrained from the bed to the upper sheet flow layer during the crest phase, has settled down once the flow reverses. At $x = 54.5$ m, δ_s is about 1.5 mm (i.e. non-zero) during the crest-to-trough flow reversal, possibly due to the significant deposition rate (about -0.2 kg/m^{2}s) of suspended sediment at this location during this phase of the wave cycle (van der Zanden et al., 2017).

At both locations, the non-zero δ_s around trough-to-crest flow reversal indicates that a fraction of sediment particles that have been entrained during the trough phase has not fully settled as the crest phase begins. This lagging of sheet flow layer concentration is caused by the relatively short time interval between maximum offshore and maximum onshore velocities in highly acceleration-skewed flows (Watanabe and Sato, 2004; Van der A et al., 2009; Ruessink et al., 2011). Maximum sheet flow thicknesses at both locations are higher during the crest than during the trough phase. Especially at $x = 53.0$ m (breaking point), where highest wave steepness and near-bed acceleration skewness were measured, a large mobilization of sand particles which contributes to onshore transport occurs during the wave crest phase. Such asymmetry in sheet flow thickness has been shown before for positively velocity- and acceleration-skewed flow conditions in an oscillatory flow tunnel (Ruessink et al., 2011) and can be explained by pressure-force-induced sand mobilization under the wave front (Drake and Calantoni, 2001; Calantoni and Puleo, 2006) and to a higher bed shear stress during the crest phase (van der A et al., 2011). Which of these two processes is dominant in the present experiment, cannot be concluded based purely on these measurements but would require a detailed numerical assessment of all forces, which besides the fluid-particle forces also includes the inter-particle interaction forces (c.f. Drake and Calantoni, 2001; Calantoni and Puleo, 2006).

To assess whether wave breaking affects the sheet flow layer thickness, δ_s is quantitatively compared with predictions by two empirical formulations for maximum δ_s that have been proposed on the basis of detailed laboratory measurements using well-sorted sand and regular oscillatory and wave conditions: firstly, the formulation by Ribberink et al. (2008) based on oscillatory flow tunnel data:

$$\delta_s/D_{50} = 10.6\,\theta, \tag{5}$$

and secondly, Schretlen's (2012) formulation based on uniform non-breaking waves measurements:

$$\delta_s/D_{50} = 13.1\,\theta^{0.7} \tag{6}$$

The Shields parameter θ is the non-dimensional bed shear by phase-averaged velocities, i.e. $\theta = \tau_b/(\rho_s - \rho)gD_{50}$, with ρ_s (=2650 kg/m^3) and ρ (=1000 kg/m^3) being the densities of sediment particles and water, respectively, and g (=9.81 m/s^2) is the gravitational acceleration. The bed shear stress τ_b is estimated based on the horizontal velocity at $\zeta = \delta$ through $\tau_b = 0.5 f_{wc} u(\delta)^2$. The methodology described by Ribberink (1998) is applied to calculate the wave-plus-current friction factor f_{wc} as a linear combination of the wave friction factor f_w and the current friction factor f_c. The wave friction factor f_w is calculated based on the widely used formulation by Swart (1974):

$$f_w = 0.00251 \exp\left[5.21\left(2\frac{T_a}{T_{hc}}\right)^{-0.49}\left(\frac{a}{k_{sw}}\right)^{-0.19}\right], \tag{7}$$

with k_{sw} being the bed roughness, calculated iteratively as a function of the Shields parameter (see Ribberink, 1998). The parameter T_a/T_{hc} is the relative time duration of accelerating flow within a half-cycle, which can be used to account for acceleration skewness effects on the bed shear stress (da Silva et al., 2006; van der A et al., 2013). In the present study, T_a/T_{hc} equals approximately 0.3 during the crest phase and 0.6 during the trough phase. This yields friction factors f_w that are approximately 30% higher for the crest phase and approximately 6% lower for the trough phase compared to f_w calculated without acceleration-skewness correction (i.e. $T_a = 0.5$ in Eq. (7)). The maximum bed shear θ_{max} and sheet flow thickness δ_s are derived per half cycle and for each 15-min stage of bar development, yielding a total of 24 data points. For the D_{50}, a constant value of 0.25 mm (from sieving tests) was used for all runs. Using the locally measured D_{50} at the end of the experiment (by laser-diffraction particle sizer) in the calculations would result in θ_{max} values that are 10–20% higher.

Fig. 7 shows measured δ_s versus θ_{max}, for θ calculations without (panel a) and with (panel b) acceleration skewness corrections. The measured data cluster around the predictions by Eqs. (5) and (6). This suggests that δ_s in the present breaking-wave conditions is consistent with previous observations in oscillatory flow tunnel and non-breaking wave conditions, despite effects of the sloping bed, the presence of breaking-generated turbulence in the WBL, and the non-uniformity of the flow. Without acceleration skewness correction, the measured crest-phase δ_s values tend to be slightly higher than the empirical predictions (Fig. 7a). When acceleration skewness effects are corrected for through T_a/T_{hc} in Eq. (7), the estimated crest-phase θ increases while the trough-phase θ decreases. In that case, the agreement between measured and predicted δ_s decreases for Eq. (5) (from $r^2 = 0.30$ to 0.23) but increases for Eq. (6) (from $r^2 = 0.42$ to 0.49).

4.3. Sheet flow particle velocities and fluxes

Particle velocities $u_p(\zeta)$ across the sheet flow layer were estimated for CCM$^+$ tank 1 at $x = 54.5$ m through cross-correlation of concentration measurements by two probes aligned in wave direction (see Section 2.5). Inherent to the applied CCM cross-correlation technique is that reliable estimates of particle velocities can only be obtained when the sheet flow layer is well-developed (c.f. Dohmen-Janssen and Hanes, 2002). Because the sheet flow layer in the present study is rather thin, u_p could only be measured around instances of maximum onshore/offshore velocity. We focus here on the final run (t = 75–90 min) when near-bed velocities were highest and the best measurements of u_p were obtained.

Fig. 8a shows phase-averaged particle velocities for t = 75–90 min. Reliable estimates of u_p were obtained for phases with δ_s roughly exceeding 4 mm. The particle velocities are in phase with near-bed water velocity and increase in magnitude with distance away from the bed.

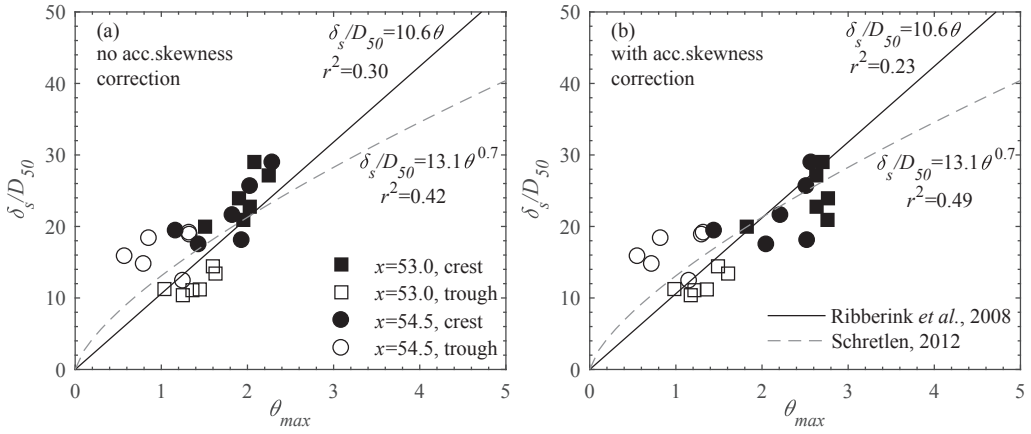

Fig. 7. Maximum sheet flow layer thickness versus maximum Shields stress per wave half-cycle, without (a) and with (b) acceleration skewness correction in calculations of θ. Also included are empirical relations proposed by Ribberink et al. (2008) (Eq. (5); solid line) and Schretlen, 2012 (Eq. (6); dashed line).

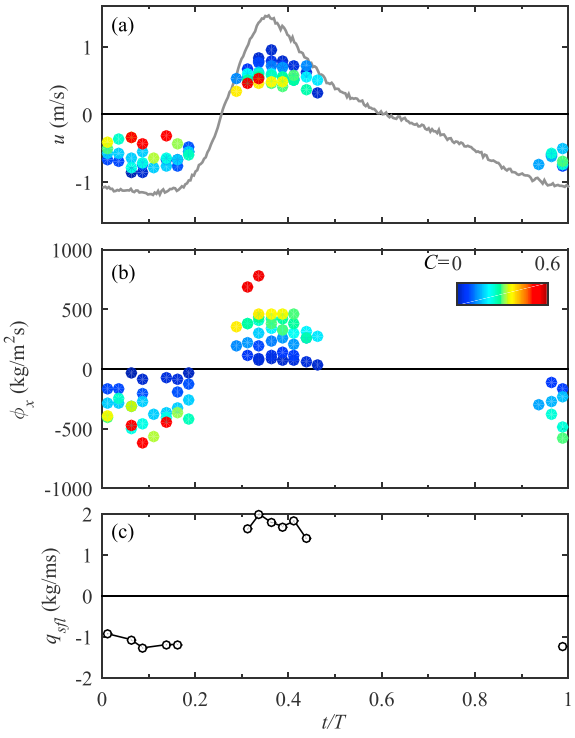

Fig. 8. Sheet flow particle velocities and sediment fluxes measured with CCM$^+$ at $x = 54.5$ m, for $t = 75$–90 min (a) ACVP-measured velocities at $\zeta = \delta$ (line) and particle velocities measured with CCM$^+$ for eight concentration bin classes (circles, with color coding indicating the volumetric concentration, see color bar in panel b); (b) Flux measurements, as product of CCM$^+$-measured particle velocities and concentrations; (c) Time-varying depth-integrated transport over the sheet-flow layer. (For interpretation of the references to colour in this figure legend, the reader is referred to the web version of this article.)

Magnitudes of u_p are typically about 40–70% of the near-bed flow velocity at $\zeta = \delta$. These relative magnitudes and the vertical structure are both consistent with previous observations of oscillatory sheet flows (e.g. McLean et al., 2001; Dohmen-Janssen and Hanes, 2002, 2005).

The particle velocities were multiplied with corresponding concentrations to obtain horizontal sediment fluxes ϕ_x (Fig. 8b). Highest sediment fluxes are found deep in the erosion layer because concentrations increase rapidly towards the bed while the vertical decay of velocities is much more gradual. Note that flux magnitudes in the sheet flow layer (100–500 kg/m^{2}s) are orders of magnitude higher than horizontal suspended sediment fluxes measured just above the WBL at the same location (1–10 kg/m^{2}s) (van der Zanden et al., 2017).

The time-varying total transport $q_{sfl}(t)$ was estimated as the depth-integrated product of measured concentrations C and estimated particle velocities u_p over the sheet flow layer, i.e. from the erosion depth z_e to the top of the upper sheet flow layer z_t:

$$q_{sfl}(t) = \int_{z_e}^{z_t} u_p(\zeta, t) C(\zeta, t) d\zeta. \quad (8)$$

The full $u_p(\zeta, t)$ profile was obtained by fitting an empirical power-law distribution, proposed by Sumer et al. (1996), through the measurements:

$$u_p(\zeta) = m \cdot \zeta^n, \quad (9)$$

with m and n as fitting parameters. Eq. (9) was log-fitted for each phase with a minimum of three $u_p(\zeta)$ measurements and accepted only if $n > 0$, yielding fitted $u_p(\zeta)$ profiles for 12 out of 40 wave instants with an average $r^2 = 0.62$. The accordingly obtained velocity distributions may not be fully correct but are considered sufficiently accurate for estimating the magnitude of $q_{sfl}(t)$.

Results of $q_{sfl}(t)$ in Fig. 8c show that instantaneous transport rates during the crest phase exceed those during the trough phase with about 50%. This is consistent with δ_s being larger during the crest phase. Indeed, Fig. 8b shows that sediment fluxes associated with a particular concentration are of similar magnitude during trough and crest phase. Hence, the vertical profile of horizontal fluxes is of similar shape during both crest and trough phase, and the larger sheet flow thickness during the crest phase leads to flux profiles that are vertically stretched and yield larger transport rates. It is further interesting to note that $q_{sfl}(t)$ is of O(1–2 kg/ms), which is of similar magnitude as the depth-integrated outer-flow suspended load transport $q_s(t)$ at this location (approximately 2.0 (±0.2) kg/ms, van der Zanden et al., 2017).

Averaging $q_{sfl}(t)$ over the wave period yields a rough approximation of the time-averaged transport in the sheet flow layer $\overline{q_{sfl}}$, excluding transport contributions around flow reversals when u_p could not be measured. Estimated $\overline{q_{sfl}} = 0.03$ (±0.1) kg/ms, i.e. the net transport over a wave cycle is two orders of magnitude lower than the instantaneous transport rate during the half cycles.

4.4. Net bedload transport rates

The total net (i.e. wave-averaged) transport rate q_{tot} is formed by a depth-integrated suspended load (q_s) and a bedload (q_{bed}) contribution. Direct measurement of q_{bed} in oscillatory conditions is generally very difficult, because the transport is confined to layers of O(sub-mm) which cannot be accurately resolved by most measuring instruments. The CCM$^+$ is one of the few instruments capable of measuring q_{bed} in sheet flow

conditions, provided that sheet flow layers are sufficiently developed ($\delta_s > 4$ mm). Most previous laboratory studies focusing on bedload transport rates could assume negligible suspended load transport (i.e. $q_{bed} \approx q_{tot}$), allowing quantification of q_{bed} from bed profile measurements (i.e. through Eq. (3)). However, because the breaking waves in the present study bring large amounts of sediment into suspension, q_s cannot be neglected. Following previous surf zone studies (Grasmeijer and Van Rijn, 1997; van der Werf et al., 2015), q_{bed} is estimated at each location as the difference between the measured total transport (Eq. (3)) and the measured suspended transport rates:

$$q_{bed}(x) = q_{tot}(x) - q_s(x) = q_{tot}(x) - \int_{z_a}^{\eta_{crest}} \overline{u(x,\zeta)C(x,\zeta)}d\zeta. \quad (10)$$

The net suspended transport rate q_s is the time-averaged cross-shore sediment flux, depth-integrated from a near-bed reference elevation z_a that defines the boundary between the bedload layer ($\zeta < z_a$) and the suspension layer ($\zeta > z_a$) up to wave crest level η_{crest}. The reference elevation $z_a = 0.005$ m, which roughly equals the maximum elevation of the sheet flow layer across the test section. Between $\zeta = z_a$ and 0.10 m, the ACVP measured the instantaneous flux through collocated u and C, enabling direct quantification of the net total flux $\overline{uC}$ including contributions of the wave-related flux $\overline{\tilde{u}\tilde{C}}$ and the turbulent diffusive flux $\overline{u'C'}$. The latter is resolved up to a 5 Hz frequency, hence capturing the contributions by the largest vortices that likely contribute most to net diffusion. For the present experiment, contributions of $\overline{\tilde{u}\tilde{C}}$ and $\overline{u'C'}$ were generally only significant inside the wave bottom boundary layer ($\zeta < \delta \approx 0.02$ m); at outer-flow elevations ($\zeta > \delta$) the net total flux was almost fully due to the current-related contribution, i.e. $\overline{uC} \approx \overline{\bar{u}\bar{C}}$. Therefore, for $\zeta > 0.10$ m, the net flux was estimated based on inter- and extrapolated vertical profiles of the time-averaged velocity (ADV measurements) and sand concentration (TSS measurements). More details on the calculation of q_s are given by van der Zanden et al. (2017).

The possible sources of measurement errors for q_s and q_{bed} are addressed in Section 7 (Discussion). Based on the variability between measurements taken at the same location but for six different runs, the measurement uncertainties of q_s and q_{bed} transport were both estimated as 0.04 kg/ms = $1.5{\cdot}10^{-5}$ m^2/s on average. These estimates include the variability due to the morphologic feedback by the bed profile evolution on the transport rates during the experiment.

Fig. 9a presents q_{bed} across the breaker bar. The figure includes the time-averaged sheet flow layer transport measured with the CCM$^+$, $\overline{q_{sfl}}$ = 0.03 kg/ms. Note the wide error margins (±0.1 kg/ms) of this measurement, which illustrate the difficulties of obtaining direct measurements of bedload transport rates. At this location, Eq. (10) yields $q_{bed} = 0.07$ (±0.04) kg/ms, which is close to the estimated $\overline{q_{sfl}}$ and within the latter's error margins. The bedload transport rates (Fig. 9a) can be explained in terms of hydrodynamic parameters, i.e. the onshore and offshore phase-averaged velocity (Fig. 9b), the dimensional periodic velocity skewness $\overline{\langle\tilde{u}^3\rangle}$, and the dimensional acceleration skewness $-\overline{\mathrm{H}(\langle\tilde{u}\rangle)^3}$ (where H is the Hilbert transform, see e.g. Elgar, 1987; Henderson et al., 2004) (Fig. 9c).

At $x = 51.0$ m, q_{bed} is positive (i.e. onshore), which is explained by the strong velocity- and acceleration-skewness of near-bed velocities and the relatively low magnitude of time-averaged undertow velocities (Table 2). Note that this location corresponds roughly to the location of maximum q_{tot} as obtained from bed profile measurements (Fig. 5). Magnitudes of q_{bed} are similar at $x = 53.0$ m (below break point), where the dimensional acceleration skewness is maximum. Towards the bar crest

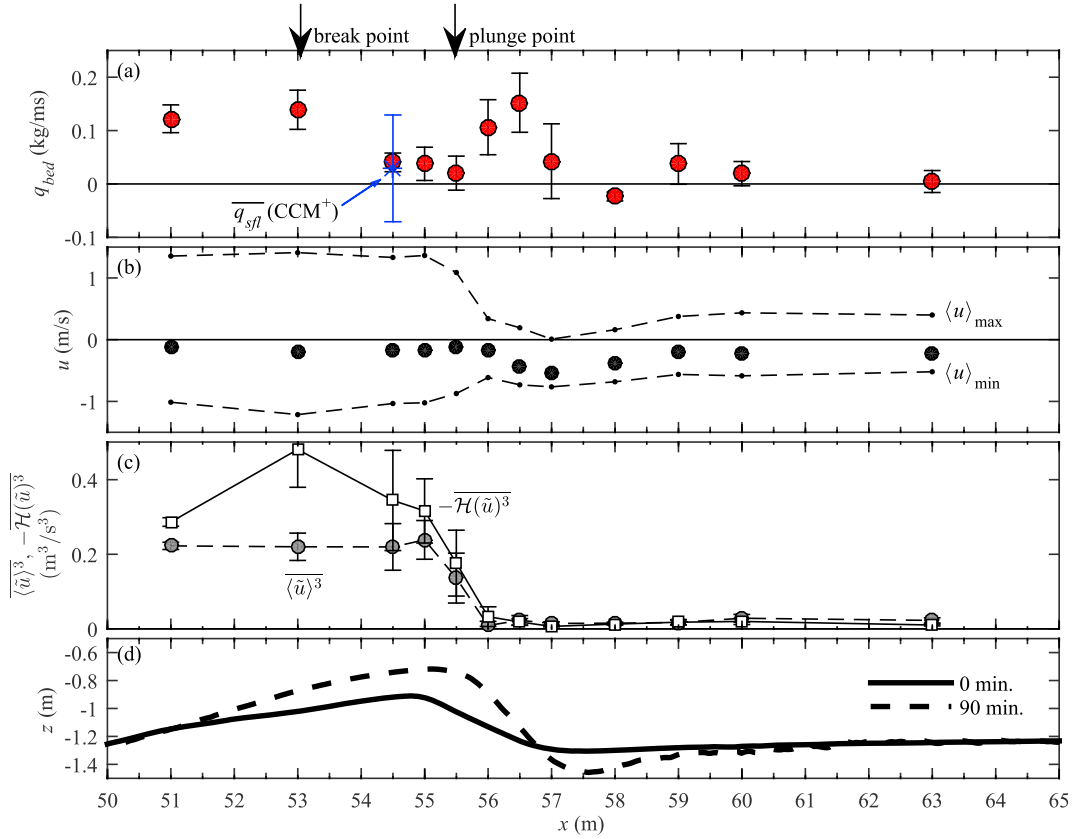

Fig. 9. Bedload transport rates across the bed profile. (a) q_{bed}, mean (circles) plus 95% confidence interval (error bars) over six runs per location. Also included is the time-averaged sheet flow transport measured with CCM$^+$ at $x = 54.5$ m for $t = 75$–90 min (star symbol, with error bars indicating the estimated error = ±0.1 kg/ms); (b) Horizontal velocity at the WBL overshoot elevation, time-averaged (black circles) and maximum onshore and offshore phase-averaged (dots and dashed lines) for $t = 0$–90 min; (c) Dimensional velocity skewness (circles) and dimensional acceleration skewness (squares) at the WBL overshoot elevation, mean values over six runs plus 95% confidence interval (error bars); (d) Bed profiles at start (solid) and end (dashed) of experiment.

($x = 54.5$–55.0 m), q_{bed} decreases, which may be caused by the decrease in acceleration skewness (compared to $x = 53.0$ m) and the increase in offshore-directed undertow magnitude (compared to $x = 51.0$ m).

Shoreward from the plunge point and along the lee-side slope of the bar, q_{bed} increases significantly. Note that $q_{bed} > 0$ while near-bed velocities are predominantly negative. Hence, the onshore transport is likely due to the large steepness of the bar, which approaches the natural angle of repose and induces downward (onshore) bedload transport by gravity. The transported grains partly accumulate at the steep offshore-facing front of the bed forms at this region, which contributes to the progressive offshore migration of these bed forms across the bar slope (see Section 3.2). The breaker trough ($x = 58.0$ m) is the only location where q_{bed} is directed offshore. This is explained by the combination of the positive bed slope dz_{bed}/dx and the strong offshore-directed undertow velocities relative to periodic velocities. Further shoreward, at the inner surf zone ($x = 59.0$–63.0 m), q_{bed} is again shoreward-directed with magnitudes gradually approaching zero.

In order to obtain more insight in the parameters controlling the measured bedload transport rates, Fig. 10 shows scatter plots of q_{bed} versus a number of hydrodynamic parameters. The chosen parameters are the dimensional orbital velocity skewness, $\overline{\langle \tilde{u} \rangle^3}$ (Fig. 10a); the dimensional acceleration skewness, $-\overline{\mathrm{H}(\langle \tilde{u} \rangle)^3}$ (Fig. 10b); the near-bed turbulent kinetic energy k_b (Fig. 10c); and the local bed slope $-dz_{bed}/dx$ (Fig. 10d). Distinction is made between two characteristic zones along the test section, i.e. the offshore slope up to the bar crest ($x \leq 55.5$ m) and the breaking region covering the bar crest up to the bar trough ($55.5 < x < 58.5$ m). The bedload transport rates in the inner surf zone are not considered in this analysis because of the presence of bed forms and the associated variability in bed roughness. In what follows, coefficients of determination (r^2) are calculated based on a linear regression between the two considered parameters.

For medium-sand and plane-bed conditions, q_{bed} is expected to correlate positively with the degree of orbital velocity skewness. Fig. 10a shows q_{bed} versus $\overline{\langle \tilde{u} \rangle^3}$ and includes a linear trend line that was found by Schretlen (2012) for medium sand ($D_{50} = 0.25$ mm) under non-breaking second-order Stokes waves. Between $x = 51.0$ and 55.5 m, measured q_{bed} in the present study is of similar magnitude as the observations for non-breaking waves by Schretlen (2012). The scatter in measured q_{bed} is addressed to measuring uncertainties and to effects by other hydrodynamic parameters than $\overline{\langle \tilde{u} \rangle^3}$. The transport rates along the shoreward bar slope (between $x = 56.0$ and 58.5 m) deviate clearly from the trend line, suggesting that other forcing parameters than $\overline{\tilde{u}^3}$ are significant at these cross-shore locations.

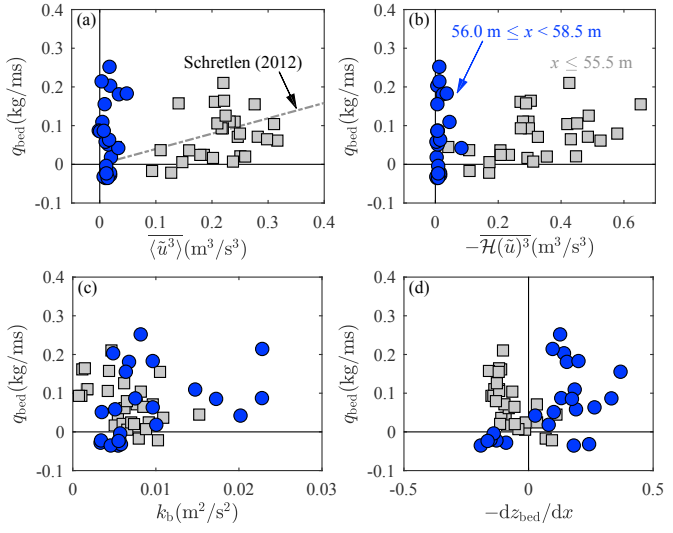

Fig. 10. Scatter plot between bedload transport and near-bed hydrodynamic parameters for 6 runs at 12 cross-shore locations (72 data points). Explaining parameters are (a) periodic velocity cubed; (b) dimensional acceleration skewness through Hilbert transform $-\mathrm{H}(\tilde{u})^3$; (c) time-averaged TKE in WBL; (d) local bed slope. Velocity variables (a–b) are obtained at overshoot elevation $\zeta = \delta$. Distinction is made between measurements along offshore bar slope to bar crest ($x \leq 55.5$ m; squares) and between bar crest and bar trough ($56.0 \leq x < 58.5$ m; circles).

A positive correlation between q_{bed} and the dimensional acceleration skewness is expected based on previous sheet flow transport measurements (c.f. van der A et al., 2010). Fig. 10b shows that between $x = 51.0$ and 55.5 m, q_{bed} indeed correlates positively with $-\mathrm{H}(\langle \tilde{u} \rangle)^3$. However, the data points in the breaking region along the shoreward bar slope ($x = 56.0$–58.5 m) do not satisfy the overall trend.

As shown by Sumer et al. (2003), an increase in near-bed TKE can lead to increased q_{bed} magnitudes. Therefore, Fig. 10c shows the scatter of q_{bed} versus the turbulent kinetic energy inside the WBL, k_b. The figure indeed suggests a positive relation between q_{bed} and k_b in the wave breaking region between $x = 56.0$ and 58.5 m, but the correlation is weak ($r^2 = 0.13$; significant at $P < 0.10$ but not at $P < 0.05$).

Gravity favors downslope bedload transport, i.e. a positive relation between q_{bed} and $-dz_{bed}/dx$ is expected. Fig. 10d indeed shows a positive correlation ($r^2 = 0.24$; significant at $P < 0.05$) between both variables for the observations between bar crest and bar trough ($x = 56.0$–58.5 m). This region involves the locations along the shoreward-facing bar slope, where particularly steep local bed slopes with a substantial effect on bedload transport are found. Note that although the locations between $x = 56.0$ and 58.5 m are characterized by simultaneously high $-dz_{bed}/dx$ and k_b, these two forcing parameters did not reveal significant correlation ($r^2 = 0.04$; $P < 0.10$) for this subset of measurements, suggesting that both parameters are statistically independent. Fig. 10d also reveals a negative relation between $-dz_{bed}/dx$ and q_{bed} for the locations offshore from the bar crest ($x \leq 55.5$ m) (significant at $P < 0.05$). This suggests that onshore bedload transport increases for steeper shoreward-tilted bed slopes, which is physically unlikely. The positive correlation between $-dz_{bed}/dx$ and q_{bed} is instead explained by positive covariance between $-dz_{bed}/dx$ and the aforementioned forcing parameters $\overline{\langle \tilde{u}^3 \rangle}$ and $-\mathrm{H}(\langle \tilde{u} \rangle)^3$ ($r^2 = 0.25$ and 0.29, respectively; both significant at $P < 0.05$).

5. Contributions of transport components to bar morphodynamics

5.1. Bedload and suspended load contributions to total transport

Fig. 11a shows the cross-shore variation of the net (i.e. wave-averaged) bedload ($\zeta < z_a = 0.005$ m) and the net depth-integrated suspended load ($\zeta > z_a$) transport rates. The net suspended load transport is further decomposed into a current-related ($q_{s,c}$) and wave-related component ($q_{s,w}$). The latter was measured with ACVP, and was generally confined to the WBL and onshore-directed (van der Zanden et al., 2017). Fig. 11b shows the relative importance f_{rel} of these three components to total transport, calculated as the relative contribution to the sum of the absolute value of individual components (e.g. for bedload, $f_{rel} = |q_{bed}|/(|q_{bed}| + |q_{s,c}| + |q_{s,w}|)$).

At the most offshore shoaling location ($x = 51.0$ m), transport is almost fully (>90%) attributed to bedload. This location is hardly affected by breaking-generated TKE and suspended sediment pick-up rates are low. Towards the crest of the bar, between the break point ($x = 53.0$ m) and plunge point ($x = 55.5$ m), the offshore-directed suspended transport gains importance over bedload transport, i.e. q_s increases while q_{bed} decreases. At these locations the onshore-directed wave-related suspended load contribution ($f_{rel} = 10$–20%) is also significant.

Along the lee side of the bar and shoreward from the plunge point ($x = 56.0$–57.0 m), both q_s and q_{bed} increase in magnitude. Magnitudes of offshore-directed q_s exceed those of onshore-directed q_{bed} by about a factor 2 ($f_{rel} \approx 0.7$ for q_s; $f_{rel} \approx 0.3$ for q_{bed}). The physical explanations for the increase in both transport components are notably different: q_s increases due to the combination of strong near-bed undertow velocities

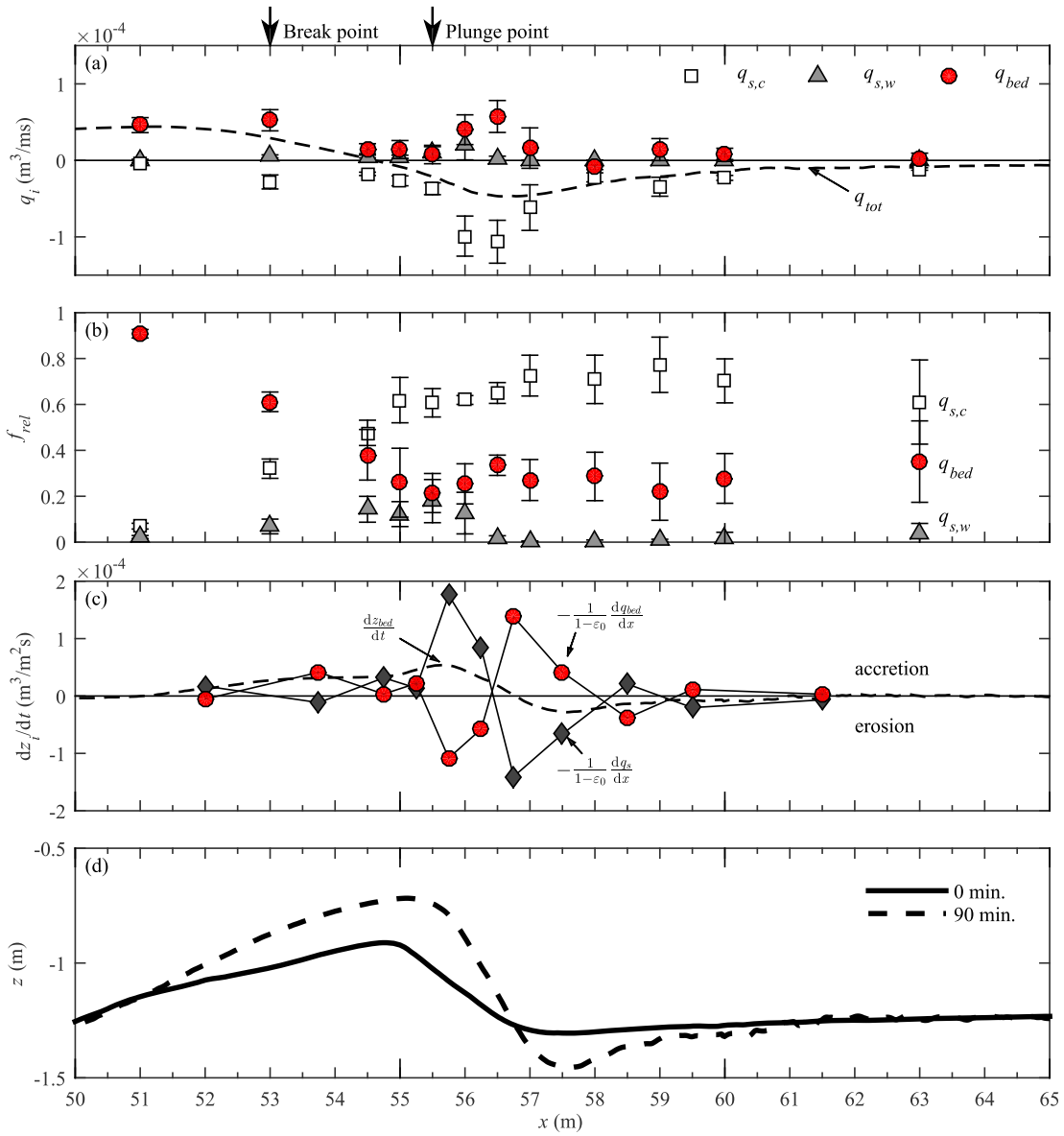

Fig. 11. Cross-shore variation in net (wave-averaged) transport rates. (a) Net transport rates along test section: total transport (dashed black line), current-related suspended transport (squares), wave-related suspended transport (triangles), and bedload (circles); (b) Relative contribution of each component to total transport, calculated as individual contribution to the sum of absolute values of the three terms (see text in Section 5.1); (c) Contributions by each component to bed level change (erosion/accretion), quantified through horizontal transport gradients divided by relative sand fraction in loosely packed bed (1 - ε_0): contributions by suspended load (wave- plus current-related, diamonds), bedload (circles) and total transport (dashed line); (d) Bed profiles at $t = 0$ and 90 min. Values in (a–c) are means over six runs, with error bars in a-b marking 95% confidence interval.

and enhanced sediment pick-up by breaking-generated turbulence, while q_{bed} increases primarily due to bed slope effects. Further shoreward at bar trough and inner surf zone locations ($x \geq 58.0$ m), both transport components decrease in magnitude and the established relative contributions by q_s ($f_{rel} \approx 0.7$) and q_{bed} ($f_{rel} \approx 0.3$) remain approximately constant.

5.2. Bedload and suspended load transport contributions to breaker bar development

Fig. 11c shows the negative cross-shore gradients (–d/dx) of q_s and q_{bed}, divided by the sediment fraction in a loosely packed bed ($1 - \varepsilon_0$; with porosity $\varepsilon_0 = 0.4$). These terms can be interpreted as the contributions by both transport components to local bed level changes. The signs are chosen such that positive values correspond to net local accretion, and negative values to net erosion, of the bed.

Suspended transport leads to erosion of the bar trough ($x = 56.5$–58.0 m) and accretion of the bar crest and higher ends of the shoreward bar slope ($x = 54.0$–56.5 m). Bedload transport leads to accretion of the breaker bar ($x = 52.0$–55.5 m), erosion of the shoreward bar slope ($x = 55.5$–56.5 m) and accretion of the breaker trough ($x = 56.5$–58.0 m). Hence, the net bed level change between $x = 55.0$ and 58.0 m (bar crest to bar trough) is explained by the net difference between opposite contributions by suspended load and bedload. Suspended load transport contributions to the bar morphodynamics exceed those by bedload, which explains the growth of the bar crest and deepening of the bar trough during the experiment.

Fig. 12 shows the suspended load (panel a) and bedload (panel b) transport rates again, but this time as a vector plot along the bar profile and in combination with their effects on local bed level changes. The figure illustrates how sediment advection occurs as suspended and bed load in opposite directions, and how both components lead to local bed erosion or accretion. Suspended transport particularly reveals net sediment pick-up in the bar trough. Once entrained, suspended grains are advected offshore and upwards along the shoreward slope of the breaker

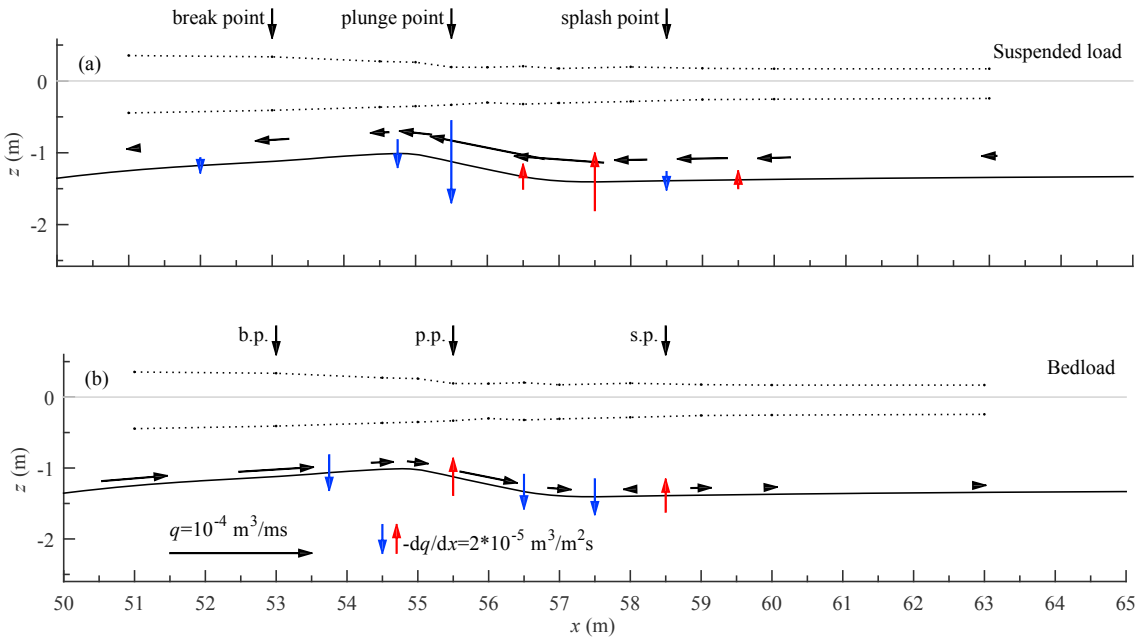

Fig. 12. Vector plot of transport rates and transport gradients, time-averaged over $t = 0$–90 min, of depth-integrated suspended load (panel a) and bedload (panel b) transport. Bed-parallel arrows (black) denote cross-shore transport rates, consistent with Fig. 11a. Vertical arrows are cross-shore gradients of each transport component, with red (upward) indicating a positive gradient dq/dx (corresponding to local erosion) and blue (downward) corresponding to negative dq/dx (local accretion). The bed profile (solid black line) is at $t = 0$ min. Transport gradients with magnitudes $<1.0{\cdot}10^{-5}$ m^3/m^2s were truncated for illustration purposes. (For interpretation of the references to colour in this figure legend, the reader is referred to the web version of this article.)

bar by the undertow. The offshore-directed suspended transport increases in offshore direction along the shoreward slope of the bar, due to the concurrent strong undertow and enhanced entrainment by breaking-generated TKE (van der Zanden et al., 2017). Suspended sediment is deposited at the bar crest where both undertow magnitudes and TKE levels decrease (compared to shoreward locations).

Bedload transport rates are large at shoaling locations ($x = 51.0$ and 53.0 m) and reduce towards the breaker bar. This leads to net sediment deposition by bedload transport between the break point and the bar crest ($x = 53.0$–54.5 m). Bedload transport rates increase along the lee-side slope of the bar, due to the steep bed slope and possibly because of increased near-bed TKE levels. It is also possible that the high q_{bed} at $x \approx 56.0$ m is partly due to the vertical influx by net settling of suspended grains at $x = 55.0$–56.0 m (Fig. 12a); these grains are already mobilized and are likely to be transported (as bedload) more easily than the grains contained in the bed. The bedload transport between $x = 55.0$ and 57.5 m leads to erosion of the bar crest and accretion of the bar trough (Fig. 12b) and counterbalances a large part of the bar accretion induced by the suspended sediment transport (Fig. 12a).

6. Grain-size sorting

This section examines the vertical grain-size sorting in suspended sediment (Section 6.1) and the cross-shore sorting along the bed surface of the breaker bar (Section 6.2). The latter is related to size-selective transport as bedload and suspended load.

6.1. Vertical sorting of suspended sediment

Fig. 13 shows vertical profiles of the median diameter (D_{50}) of suspended sediment, sampled with a six-nozzle Transverse Suction System (TSS). Profiles of D_{10} and D_{90} are qualitatively similar and are not shown here for brevity. Different behavior is observed for locations relatively far offshore/shoreward from the plunge point, i.e. at the shoaling location $x = 51.0$ m and at inner surf-zone locations $x = 59.0$–63.0 m, versus the locations in the breaking region ($x = 53.0$–58.0 m).

At the shoaling and inner surf zone, it is firstly shown that the D_{50} of particles in suspension is substantially lower than the mean D_{50} in the flume (grey line). Secondly, vertical sorting occurs, as the suspended sediment becomes finer with distance from the bed. At inner surf zone locations ($x > 58.5$ m), the D_{50} at the highest TSS nozzle ($\zeta = 0.53$ m) is systematically larger than the D_{50} measured closer to the bed (at $\zeta = 0.31$ m). A possible explanation is that the sand fraction at $\zeta = 0.53$ m contains a larger fraction of sediment that is entrained in the breaking region and then advected to the inner surf zone at elevations above wave trough level (see van der Zanden et al., 2017). Similarly, the suspended sediment at $x = 51.0$ m is not necessarily entrained locally, but may instead consist of the finest fractions of sediment particles that are picked up in the breaking region and then advected offshore.

In the breaking region ($x = 54.5$–58.0 m), large suspended sediment concentrations were found up to the water surface due to large pick-up rates and strong vertical mixing (van der Zanden et al., 2017). Fig. 13 shows little vertical segregation in D_{50} for this region, especially for the locations ± 1 m from the plunge point (at $x = 55.5$ m). The suspended sediment appears to be well-mixed and also the coarsest particles are carried to high elevations (up to water surface). Moreover, the D_{50} of suspended sediment is almost the same as the mean D_{50} of the initial bed.

The different sorting behavior for shoaling and inner surf zone versus the breaking region can be related to the processes responsible for sediment pick-up and vertical mixing. Davies and Thorne (2016) detail how for vortex-rippled beds, vertical mixing of particles is due to combined convection (by relatively large coherent periodic vortices ejected from the bed) and diffusion (by random turbulent fluctuations). Convection becomes increasingly important in terms of sediment entrainment and mixing for the coarser fractions in a sediment mixture (Davies and Thorne, 2016). At the shoaling and inner surf zone, turbulent vortices are primarily bed-generated and have a relatively small time and length scale. These small vortices lead to size-selective pick-up and also to vertical segregation of suspended sediment due to differences in vertical mixing and settling for each sediment size fraction, as shown for sheet flow conditions in an oscillatory flow tunnel (Hassan, 2003) and for rippled beds under uniform non-breaking waves (Sistermans, 2002; Davies and Thorne, 2016). In the wave breaking region, turbulent vortices are of larger scale and are more energetic, i.e. have a strong

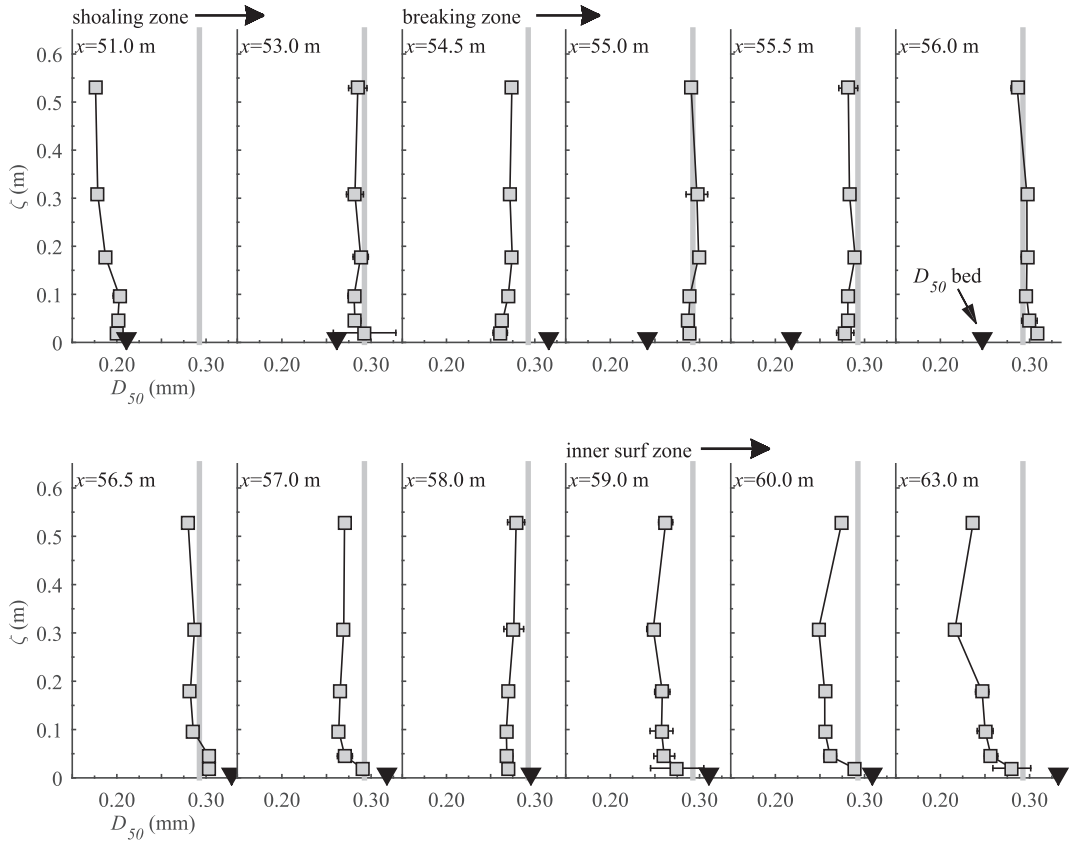

Fig. 13. Vertical profiles of median diameter (D_{50}) of suspended sediment particles at the 12 measurement locations. Markers denote means (squares) and 95% confidence interval (horizontal error bars) over six runs ($t = 0$–90 min). Black triangles denote the measured D_{50} of the bed at the end of the experiment ($t = 90$ min). Vertical grey lines denote the mean D_{50} of the original bed.

convective mixing capacity for a broad particle size range. Consequently, vertical sorting in suspended sediment particle size is restricted under breaking waves (see also Wang et al., 1998).

6.2. Cross-shore sorting in the bed

Fig. 14 shows the cross-shore variation in D_{50} of bed samples for three stages of bar development. Starting with an almost homogeneous grain-size distribution along the test section, evident size-sorting occurs throughout the experiment, resulting in a distinct pattern of grain distribution at the end of the experiment.

At the locations along the offshore slope of the bar ($x = 51.0$–54.0 m), the D_{50} decreases in time. Considering the bedload and suspended load transport patterns (as discussed in the previous sections), the temporal evolution in D_{50} can be related to two processes: first, net removal of the coarsest grains in the mixture through selective sheet flow transport (de Meijer et al., 2002; Hassan and Ribberink, 2005); second, the net deposition of fine suspended particles that are advected offshore from the inner surf and breaking zone, particularly by the undertow (c.f. Sistermans, 2002). The second process (offshore transport of fine particles) also explains the measured coarsening of the bed at inner surf zone locations ($x > 58.5$ m). This leads to an overall trend of increasing D_{50} from shoaling to inner surf zone.

The region around the breaker bar does not obey this overall trend; additional sorting mechanisms seem relevant. Slightly offshore from the bar crest (at $x = 54.5$ m) the D_{50} increases, which can be related to the transport of relatively coarse particles as sheet flow, which are deposited at the bar crest (see also Fig. 12). Slightly shoreward, at the bar crest and the highest elevations along the bar lee side ($x = 55.0$–56.0 m), the diameter decreases. Net deposition of suspended grains occurs at these locations (see Fig. 12). However, at these locations the grain size of suspended particles is significantly coarser than the particles forming the bed (Fig. 13) and consequently, this deposition cannot explain the decreasing D_{50} in the bed. Instead, it is explained by the gravity-driven bedload transport along the steep lee-side of the breaker bar (Fig. 12). Coarser grains in a sediment mixture have a larger tendency to be transported downslope than finer grains (lee-side sorting). This downslope coarsening along slopes has been shown by several studies in steady flow conditions (see Kleinhans, 2004, for an overview). The relatively coarse sediment at the breaker trough ($x = 56.5$–58.0 m) supports this explanation.

7. Discussion

The present experiment focuses on an evolving breaker bar under forcing of monochromatic normal-incident waves. Although this set-up allows study of the sand transport processes driving bar growth in unprecedented detail, it should be noted that these conditions change from natural beaches where waves are irregular, flow and sand transport is alongshore non-uniform, and bed profiles are usually closer to a semi-equilibrium state. In addition, in the present bed configuration the breaker bar and trough were separated from the sloping beach by an elongated inner surf zone in order to reduce the effects of beach processes on breaker bar morphodynamics. This differs from natural beaches and from laboratory studies with plane sloping initial beds, where the bar-trough region is often more closely connected to the inner surf and swash zones. If a plane sloping bed had been used as initial bed configuration, water depths in the inner surf zone would be shallower, likely resulting in a higher offshore-directed suspended sand flux from the inner surf zone to the breaker trough region and a reduced erosion rate at the bar trough. Also the offshore slope affects the breaker bar morphodynamics. In the present experiment, a relatively steep slope ($\tan(\alpha) = 0.10$)

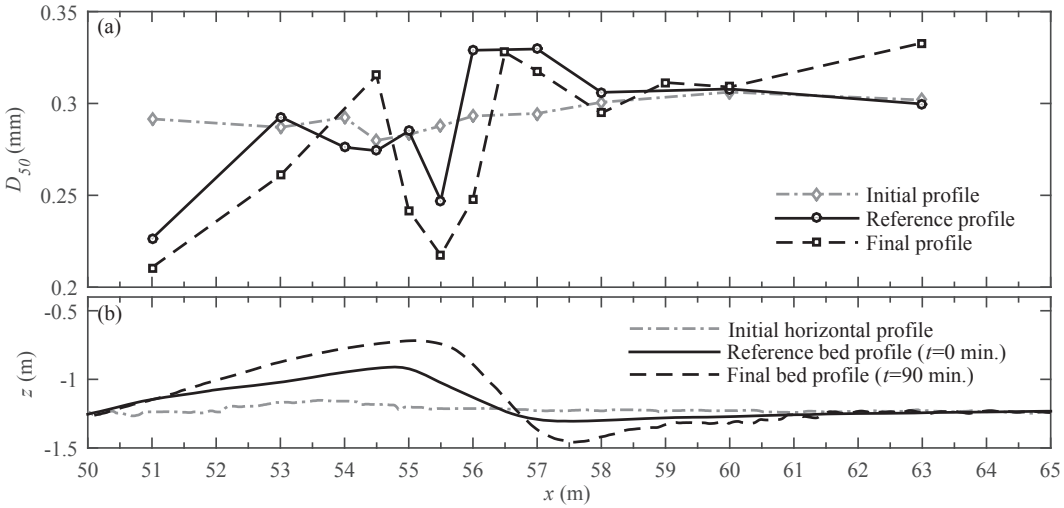

Fig. 14. (a) D_{50} sand bed (top 1–2 cm) during three stages of bed profile evolution: start of the experiment with horizontal test section (dot-dashed grey line); after initial 105-min start-up stage, i.e. reference bed profile at $t = 0$ min (solid black line); at the end of the experiment, i.e. final bed profile at $t = 90$ min (black dashed line). (b) Bed profiles corresponding to three bed development stages in (a).

was used, leading to strong wave shoaling. This in return resulted in highly cross-shore non-uniform wave shape and height in the shoaling region, which promoted the erosion of the offshore slope by bedload transport. Consequently, for a milder and more dissipative offshore slope, one may expect a reduction in erosion rates by bedload transport under the shoaling waves. Such a milder slope would also importantly change the wave breaking process and would alter the overall experimental conditions significantly.

Bedload transport rates q_{bed} are obtained indirectly by subtracting the depth-integrated suspended load q_s from the total load q_{tot} that was obtained from the bed profile evolution. Due to propagation of errors in the measurements and data treatment steps (e.g. direct measurement errors, uncertainty in the acoustic inversion methodology for ACVP-measured concentrations, uncertainties in z_{bed} and q_{tot} as detailed in Section 2.5, inter- and extrapolation of concentration and velocity profiles to estimate q_s, assumption of cross-flume uniform flow), the obtained bedload transport rates are subject to relatively large uncertainties. A quantitative indication of the random error in q_{bed} (0.04 kg/ms) was obtained by calculating the standard deviation over six runs at the same cross-shore location (see Fig. 11a). Unfortunately, these uncertainties in the estimated bedload transport rates cannot be easily overcome, because direct measurements of bedload transport rates in such a challenging measurement environment are extremely difficult with existing instrumentation. Two observations justify the use of the indirectly obtained bedload transport rates: first, the indirect estimates of q_{bed} are consistent with estimates of the wave-averaged sheet flow layer transport from CCM$^+$ measurements (Fig. 9a); second, q_{bed} scales similarly to hydrodynamic forcing as previous transport observations of medium-sand sheet flow transport by Schretlen (2012) (see Fig. 10a).

Bedload transport is defined here as the transport that occurs at $\zeta < 0.005$ m above the undisturbed bed level. This choice affects some results, for example the absolute bedload transport rate and the ratio between bedload and suspended load transport, and it requires some reflection. If the reference elevation would be raised to the WBL overshoot elevation (at $\zeta \approx 0.02$ m), the ratio between bedload and suspended load transport would not change drastically since most (80–90%) of the suspended load transport occurs at outer-flow elevations above the WBL (van der Zanden et al., 2017). Results will likely be more sensitive to a decrease in reference elevation, due to the strong vertical concentration gradient inside the sheet flow layer. Nevertheless, previous medium-sand sheet flow measurements showed that the majority of sheet flow transport is due to horizontal fluxes in the pick-up layer, i.e. at $\zeta < 0$ (Schretlen, 2012). Consequently, we do not expect the results to change drastically for other reference elevations (within the range $0 < \zeta < 0.02$ m).

The present study quantifies, possibly for the first time, the simultaneous contributions by both transport components to bed level changes across a large-scale breaker bar, and allows a detailed assessment of the governing mechanisms for bar formation mentioned in the Introduction (Dyhr-Nielsen and Sorensen, 1970; Dally and Dean, 1984; Zhang and Sunamura, 1994). The present experiment confirms the importance of suspended sand transport for bar morphodynamics. Most notably is the high local maximum in offshore-directed q_s in the breaking region between bar crest and bar trough, which is explained by concurrent high TKE and undertow magnitudes (van der Zanden et al., 2017). These observations support the numerical results of Dally and Dean (1984), who found a strong increase in q_s magnitudes in the wave breaking region due to a simultaneous increase in undertow magnitude and in suspended load, which both scale to cross-shore gradients in the wave energy (flux). The present study further supports the extensive descriptions on the effects of breaking-generated turbulent vortices on bar morphodynamics by Zhang and Sunamura (1994).

Also consistent with aforementioned bar formation mechanisms (Dyhr-Nielsen and Sorensen, 1970; Dally and Dean, 1984) is the onshore transport in the shoaling zone. However, in contrast with these studies, the onshore transport in the present experiment is not explained by near-bed suspended sand fluxes driven by onshore WBL currents, but instead, is due to bed load transport that is driven by wave skewness and asymmetry. This confirms earlier wave flume observations that suggested that onshore bed load and offshore suspended load transport rates are of similar magnitude (Grasmeijer and Van Rijn, 1997; van der Werf et al., 2015; using data of Roelvink and Reniers, 1995), and also supports studies highlighting the importance of wave skewness and asymmetry for breaker bar morphodynamics (Elgar et al., 2001; Hoefel and Elgar, 2003). The bed slope is another parameter that significantly affects bedload transport rates and bar morphodynamics in the present experiment.

Sand grains in the bed experience two fluid forces acting in cross-shore direction: an inertia or pressure force by horizontal pressure gradients dp/dx, and a drag force due to the shear stress exerted by the flow (e.g. Cox et al., 1991). For individual sand grains under surf zone waves, the drag force exceeds the inertia force by orders of magnitude (Cox et al., 1991). However, pressure forces can penetrate into the bed and can exert a force over a layer of $O(10D_{50})$ thickness, causing the sand bed to erode as a block rather than as individual grains (Zala Flores and Sleath, 1998; Sleath, 1999; Foster et al., 2006). The occurrence of such 'plug

flows' can be predicted based on the Sleath parameter $S(t) = \rho(du/dt)/(g(\rho_s - \rho))$, where ρ and ρ_s are the densities of water and sediment, respectively, and the Shields parameter θ (Foster et al., 2006; Cheng et al., 2016). At the breaking point ($x = 53.0$ m), where the wave is steepest and the highest horizontal pressure gradients are found, maximum $S = 0.30$ and maximum $\theta = 2.2$ (using Eq. (7) for f_w while excluding acceleration skewness effects, i.e. $T_a/T_{hc} = 0.5$). This is above the threshold proposed by Foster et al. (2006) based on observations under progressive surface waves (i.e. $S > 0.1$) and very close to the threshold found by Cheng et al. (2016) based on detailed numerical simulations (i.e. $0.053\theta + S > 0.426$). Nevertheless, no evidence for plug flow was found in the present study: the bed erodes layer-by-layer and not as a block, and sheet flow thicknesses are quantitatively similar to non-breaking wave and oscillatory tunnel sheet flows. In such sheet flow layers we may expect the fluid drag force to be the main driver for the horizontal transport of sand grains, although pressure forces may contribute to the initial mobilization (Calantoni and Puleo, 2006). The sheet flow layer grows due to dispersive inter-particle forces, that lead to upward transmittal of sand grains as long as the velocity shear layer (i.e. $d|u|/d\zeta > 0$) sustains (Bagnold, 1954; Sleath, 1999).

The CCM$^+$ measurements show a simultaneous concentration decrease in the sheet flow erosion layer and a concentration increase in the upper sheet flow layer. The local time-varying sediment load between $\zeta = -3$ mm and $+5$ mm, quantified through depth-integration of $\langle C(\zeta, t)\rangle$, remained at both CCM$^+$ locations roughly constant throughout the wave cycle. This confirms that the intra-wave growth and decay of the sheet flow layer is primarily due to local vertical sediment exchange processes (i.e. sediment pick-up, vertical advection and diffusion inside the sheet flow layer, and settling), with limited contributions by horizontal sediment influx from adjacent cross-shore locations. In addition, no evident effects related to the presence of breaking-generated turbulence or to the bed slope are found. Instead, the sheet flow layer thickness at the bar crest can be reasonably well predicted based on local phase-averaged velocity using existing empirical formulations that were originally developed for non-breaking wave and oscillatory flow tunnel sheet flows. It is reasonable to assume that, within the range of hydrodynamic and bed conditions examined, also existing models for sheet flow transport that are based on local velocity forcing are valid for the bar crest region in the wave breaking zone.

Interestingly, the estimated bedload transport rates along the shoreward bar slope are directed onshore, while near-bed velocities are directed offshore during almost the entire wave cycle. Hence, bed shear by phase-averaged velocities cannot be the only mobilizer of bedload particles and instead, bed slope and possibly breaking-generated TKE have significant effects (Fig. 10). Physically, the effects of breaking-generated turbulence on bedload transport are explained as follows. Small-scale wave flume observations revealed that the intermittent arrival of breaking-generated turbulence at the bed can result in instantaneous bed shear stresses in both onshore and offshore direction with magnitudes several times the time- and phase-averaged bed shear stress (Cox and Kobayashi, 2000; Sumer et al., 2013). The occurrence of such intermittent turbulence events at the bed is random, i.e. it does not correlate with a specific phase of the wave cycle (Cox and Kobayashi, 2000). The intermittent large bed shear stresses will mobilize particles which on a sloping bed will be transported downslope by gravity. Such a combined effect by TKE and bed slope may be the physical mechanism behind the observed onshore transport along the lee-side of the bar in the present study. Such transport could for instance be modeled as a separate component to bedload transport using a deterministic formulation with bed slope and breaking-generated turbulence as main input parameters (e.g. Fernández-Mora et al., 2015). Note that the correlations between bedload transport rates and forcing parameters (Section 4.4) are relatively low due to the measurement uncertainties in q_{bed} and the relatively narrow range of variation of the hydrodynamic parameters for one wave condition. Additional physical or numerical experiments would be required to further understand the effects of breaking-generated turbulence on bedload transport and to account for these effects in bedload transport models.

Although the sand was well-sorted, evident cross-shore grain size sorting was observed and could be related to size-selective transport both as bedload and as suspended load. This is consistent with combined experimental-numerical investigations of breaker bar morphodynamics for moderately sorted (Broekema et al., 2016) and bimodal sands (Srisuwan et al., 2015; Srisuwan and Work, 2015). Our study differs in that the bed and suspended load transport rates are directly inferred from the measurements and offers additional insights in local sorting processes around the breaker bar. The samples of suspended sand particles reveal size-selective pick-up and vertical sorting at the rippled-bed inner surf zone, but approximately size-indifferent entrainment and mixing in the breaking region, likely due to energetic large-scale vortices. Although existing models can reproduce the cross-shore grain sorting around laboratory breaker bars reasonably well (c.f. Srisuwan and Work, 2015; Broekema et al., 2016), the present measurements suggest that model formulations for size-selective pick-up may be further improved by accounting for the size-indifferent pick-up under plunging waves.

8. Conclusions

We present measurements of sand transport processes and transport rates along an evolving medium-sand breaker bar under a large-scale plunging breaking wave. Measurements of the sheet flow layer were obtained at two cross-shore locations near the crest of the breaker bar using CCM$^+$. Grain size sorting was studied through samples of suspended sediment and of the sand bed. The total transport rate was split into a depth-integrated suspended transport rate and a bedload transport rate, which were both assessed to obtain a complete overview of the governing transport contributions to breaker bar development. From the results we conclude:

1. The sheet flow layer near the bar crest responds quasi-instantaneously to local velocity forcing and does not reveal significant effects by breaking-generated turbulence. Wave asymmetry (velocity and acceleration skewness) leads to significantly higher sheet flow thickness during the wave crest phase than during the trough phase, especially at the wave breaking point. The sheet flow layer thickness can be adequately predicted using existing parameterizations based on local phase-averaged velocity. The time-varying transport rate depth-integrated over the sheet flow layer is of similar magnitude as the time-varying suspended sediment transport rate.
2. The net (i.e. wave-averaged) total transport rate consists of a generally onshore-directed bedload and an offshore-directed suspended load component, which are of similar magnitude. Bedload transport dominates at the shoaling zone, decreases at the bar crest, and increases again at the shoreward facing bar slope. The latter is explained by bed slope effects (i.e. gravity-driven transport) and occurs in the presence of high near-bed turbulent kinetic energy, which possibly enhances the mobilization of sand grains. Due to increased suspended sediment load and undertow magnitudes, suspended transport dominates over bedload transport in the breaking and inner surf zones. Consequently, near the plunge point the net total transport reverses from onshore-directed (shoaling zone) to offshore-directed (breaking and inner surf zone).
3. During the experiment, the breaker bar crest increases in height while the bar trough deepens. Both bedload and suspended sediment transport contribute to breaker bar morphodynamics, but their effects are notably different. Bedload transport leads to erosion of the offshore slope and accretion at the bar crest, and additionally leads to erosion of the steep shoreward bar slope and deposition at the bar trough. Suspended transport induces erosion of the bar trough, offshore and upward advection of sediment by the undertow along the shoreward bar slope, and net deposition at the breaker bar crest.

4. Suspended sediment samples show evidence of vertical grain sorting at the shoaling and inner surf zone, which indicates that sediment pick-up and vertical mixing is size-selective (i.e. the fraction of fine sediment increases with elevation). This contrasts with the breaking region, where sediment pick-up and vertical mixing is size-indifferent due to the large-scale energetic vortices (strong upward forcing). Bed samples reveal cross-shore sorting of sand particles by size-selective transport as bedload and suspended load. This sorting leads to a gradual increase in sediment size from shoaling to inner surf zone and reveals additional local sorting around the breaker bar due to bed slope effects (i.e. downward coarsening along the steep shoreward bar slope).

Measurements from the same experiment were used previously to study the effects of wave breaking on wave bottom boundary layer hydrodynamics (van der Zanden et al., 2016) and on suspended sediment processes (van der Zanden et al., 2017). All combined, the studies offer a detailed insight into the complex spatiotemporally-varying hydrodynamics and sediment dynamics along a breaker bar under a plunging wave. Upon completion of the project, the data will be disseminated to the scientific community.

Acknowledgments

The authors wish to thank the staff of CIEMLAB, in particular Joaquim Sospedra, Oscar Galego and Ricardo Torres, for their hospitality and hard work during the experimental campaign. We thank Sjoerd van Til for his contributions to the grain size analysis. The authors are also grateful to fellow SINBAD researchers for their feedback on preliminary results and to two anonymous reviewers for their constructive feedback on the draft manuscript. The research presented in this paper is part of the SINBAD project, funded by STW (12058) and EPSRC (EP/J00507X/1, EP/J005541/1). We further acknowledge the European Community's FP7 project Hydralab IV (contract no. 261520) for funding the accompanying SandT-Pro experiments.

References

Bagnold, R.A., 1954. Experiments on a gravity-free dispersion of large solid spheres in a newtonian fluid under shear. Proc. R. Soc. a: Math. Phys. Eng. Sci. 225 (1160), 49–63. http://dx.doi.org/10.1098/rspa.1954.0186.

Baldock, T.E., Alsina, J.M., Caceres, I., Vicinanza, D., Contestabile, P., Power, H., Sanchez-Arcilla, A., 2011. Large-scale experiments on beach profile evolution and surf and swash zone sediment transport induced by long waves, wave groups and random waves. Coast. Eng. 58 (2), 214–227. http://dx.doi.org/10.1016/j.coastaleng.2010.10.006.

Battjes, J.A., 1974. Surf similarity. In: Proceedings of the 14th International Conference on Coastal Engineering. American Society of Civil Engineers, Copenhagen, Denmark, pp. 466–480.

Beckman Coulter Inc, 2008. Manual LS 13 320 Particle Size Analyzer: 235.

Blott, S.J., Pye, K., 2001. GRADISTAT: a grain size distribution and statistics package for the analysis of unconsolidated sediments. Earth Surf. Process. Landf. 26 (11), 1237–1248. http://dx.doi.org/10.1002/esp.261.

Broekema, Y.B., Giardino, A., van der Werf, J.J., van Rooijen, A.A., Vousdoukas, M.I., van Prooijen, B.C., 2016. Observations and modelling of nearshore sediment sorting processes along a barred beach profile. Coast. Eng. 118, 50–62. http://dx.doi.org/10.1016/j.coastaleng.2016.08.009.

Calantoni, J., Puleo, J.A., 2006. Role of pressure gradients in sheet flow of coarse sediments under sawtooth waves. J. Geophys. Res. 111 (C1) http://dx.doi.org/10.1029/2005jc002875.

Cheng, Z., Hsu, T.-J., Calantoni, J., 2016. SedFoam: a multi-dimensional Eulerian two-phase model for sediment transport and its application to momentary bed failure. Coast. Eng. http://dx.doi.org/10.1016/j.coastaleng.2016.08.007.

Cox, D.T., Kobayashi, N., Mase, H., 1991. Effects of fluid accelerations on sediment transport in surf zones. In: Proc. Coastal Sediments, Seattle, USA, pp. 447–461.

Cox, D.T., Kobayashi, N., 2000. Identification of intense, intermittent coherent motions under shoaling and breaking waves. J. Geophys. Res. Oceans 105 (C6), 14223–14236. http://dx.doi.org/10.1029/2000JC900048.

da Silva, P.A., Temperville, A., Seabra Santos, F., 2006. Sand transport under combined current and wave conditions: a semi-unsteady, practical model. Coast. Eng. 53 (11), 897–913. http://dx.doi.org/10.1016/j.coastaleng.2006.06.010.

Davies, A.G., Thorne, P.D., 2016. On the suspension of graded sediment by waves above ripples: inferences of convective and diffusive processes. Cont. Shelf Res. 112, 46–67. http://dx.doi.org/10.1016/j.csr.2015.10.006.

de Meijer, R.J., Bosboom, J., Cloin, B., Katopodi, I., Kitou, N., Koomans, R.L., Manso, F., 2002. Gradation effects in sediment transport. Coast. Eng. 47 (2), 179–210. http://dx.doi.org/10.1016/s0378-3839(02)00125-4.

Dohmen-Janssen, C.M., Hanes, D.M., 2002. Sheet flow dynamics under monochromatic nonbreaking waves. J. Geophys. Res. 107 (C10) http://dx.doi.org/10.1029/2001jc001045.

Dohmen-Janssen, C.M., Hanes, D.M., 2005. Sheet flow and suspended sediment due to wave groups in a large wave flume. Cont. Shelf Res. 25 (3), 333–347. http://dx.doi.org/10.1016/j.csr.2004.10.009.

Drake, T.G., Calantoni, J., 2001. Discrete particle model for sheet flow sediment transport in the nearshore. J. Geophys. Res. 106 (C9), 19859. http://dx.doi.org/10.1029/2000jc000611.

Dubarbier, B., Castelle, B., Marieu, V., Ruessink, G., 2015. Process-based modeling of cross-shore sandbar behavior. Coast. Eng. 95, 35–50. http://dx.doi.org/10.1016/j.coastaleng.2014.09.004.

Dally, W.R., Dean, R.G., 1984. Suspended sediment transport and beach profile evolution. J. Waterw. Port Coast. Ocean Eng. ASCE 110 (1), 15–33. http://dx.doi.org/10.1061/(ASCE)0733-950X(1984)110:1(15).

Dalrymple, R.A., 1992. Prediction of storm/normal beach profiles. J. Water Port Coast. Ocean Eng. 118 (2), 193–200. http://dx.doi.org/10.1061/(asce)0733-950x(1992)118:2(193).

Dean, R.G., 1973. Heuristic models of sand transport in the surf zone. In: Paper Presented at the Proc. Conf. Eng. Dynamics in the Surf Zone, Sydney, Australia.

Dean, R.G., Dalrymple, R.A., 2001. Coastal Processes with Engineering Applications. Cambridge University Press.

Dyhr-Nielsen, M., Sorensen, T., 1970. Some sand transport phenomena on coasts with bars. In: Proceedings of the 12th International Conference on Coastal Engineering. Washington, D.C., vol. 54, pp. 855–865.

Elgar, S., 1987. Relationships involving third moments and bispectra of a harmonic process. IEEE Trans. Acoust. Speech Signal Process. ASSP 35 (12), 1725–1726.

Elgar, S., Gallagher, E.L., Guza, R.T., 2001. Nearshore sandbar migration. J. Geophys. Res. 106 (C6), 11623. http://dx.doi.org/10.1029/2000jc000389.

Eshel, G., Levy, G.J., Mingelgrin, U., Singer, M.J., 2004. Critical evaluation of the use of laser diffraction for particle-size distribution analysis. Soil Sci. Soc. Am. J. 68 (3), 736. http://dx.doi.org/10.2136/sssaj2004.7360.

Fernández-Mora, A., Calvete, D., Falqués, A., de Swart, H.E., 2015. Onshore sandbar migration in the surf zone: new insights into the wave-induced sediment transport mechanisms. Geophys. Res. Lett. 42 (8), 2869–2877. http://dx.doi.org/10.1002/2014gl063004.

Finn, J.R., Li, M., Apte, S.V., 2016. Particle based modelling and simulation of natural sand dynamics in the wave bottom boundary layer. J. Fluid Mech. 796, 340–385. http://dx.doi.org/10.1017/jfm.2016.246.

Foster, D.L., Beach, R.A., Holman, R.A., 2006. Turbulence observations of the nearshore wave bottom boundary layer. J. Geophys. Res. Oceans 111 (C4). http://dx.doi.org/10.1029/2004jc002838.

Grasmeijer, B.T., Van Rijn, L.C., 1997. Sand Transport over a Breaker Bar in the Surf Zone. Coastal Dynamics, Plymouth, UK, pp. 88–98.

Hassan, W.N., Ribberink, J.S., 2005. Transport processes of uniform and mixed sands in oscillatory sheet flow. Coast. Eng. 52 (9), 745–770. http://dx.doi.org/10.1016/j.coastaleng.2005.06.002.

Hassan, W.N.M., 2003. Transport of Size-graded and Uniform Sediment under Oscillatory Sheet-flow Conditions. PhD Thesis. University of Twente.

Henderson, S.M., Allen, J.S., Newberger, P.A., 2004. Nearshore sandbar migration predicted by an eddy-diffusive boundary layer model. J. Geophys. Res. 109 (C6) http://dx.doi.org/10.1029/2003jc002137.

Hoefel, F., Elgar, S., 2003. Wave-induced sediment transport and sandbar migration. Science 299 (5614), 1885–1887. http://dx.doi.org/10.1126/science.1081448.

Hsu, T.-J., Elgar, S., Guza, R.T., 2006. Wave-induced sediment transport and onshore sandbar migration. Coast. Eng. 53 (10), 817–824. http://dx.doi.org/10.1016/j.coastaleng.2006.04.003.

Hurther, D., Thorne, P.D., Bricault, M., Lemmin, U., Barnoud, J.M., 2011. A multi-frequency Acoustic Concentration and Velocity Profiler (ACVP) for boundary layer measurements of fine-scale flow and sediment transport processes. Coast. Eng. 58 (7), 594–605. http://dx.doi.org/10.1016/j.coastaleng.2011.01.006.

Kleinhans, M.G., 2004. Sorting in grain flows at the lee side of dunes. Earth Sci. Rev. 65 (1–2), 75–102. http://dx.doi.org/10.1016/s0012-8252(03)00081-3.

Koomans, R.L., 2000. Sand in Motion: Effects of Density and Grain Size. Rijksuniversiteit Groningen, The Netherlands.

Kraus, N.C., Larson, M., 1988. Beach profile Change Measured in the Tank for Large Waves 1956-1957 and 1962. US Army Corps of Engineers, Coastal Engineering Research Center. Document number CERC-88-6.

Kriebel, D.L., Dally, W.R., Dean, R.G., 1986. Undistorted Froude model for surf zone sediment transport. In: Proc. 20th Int. Conf. on Coastal Eng, Taipei, Taiwan, pp. 1296–1310.

Lanckriet, T., Puleo, J.A., Waite, N., 2013. A conductivity concentration profiler for sheet flow sediment transport. IEEE J. Ocean. Eng. 38 (1), 55–70. http://dx.doi.org/10.1109/joe.2012.2222791.

Lanckriet, T., Puleo, J.A., 2015. A semianalytical model for sheet flow layer thickness with application to the swash zone. J. Geophys. Res. Oceans 120 (2), 1333–1352. http://dx.doi.org/10.1002/2014jc010378.

Lippmann, T.C., Holman, R.A., 1990. The spatial and temporal variability of sand bar morphology. J. Geophys. Res. 95 (C7), 11575. http://dx.doi.org/10.1029/JC095iC07p11575.

McLean, S.R., Ribberink, J.S., Dohmen-Janssen, C.M., Hassan, W.N., 2001. Sand transport in oscillatory sheet flow with mean current. J. Waterw. Port Coast. Ocean Eng. 127 (3), 141–151. http://dx.doi.org/10.1061/(asce)0733-950x(2001)127:3(141).

Murray, S.P., 1967. Control of grain dispersion by particle size and wave state. J. Geol. 27 (5), 612–634.
Nielsen, P., 1984. Field-measurements of time-averaged suspended sediment concentrations under waves. Coast. Eng. 8 (1), 51–72. http://dx.doi.org/10.1016/0378-3839(84)90022-X.
Nielsen, P., 1992. Coastal Bottom Boundary Layers and Sediment Transport. World Scientific, Singapore.
O'Donoghue, T., Wright, S., 2004. Concentrations in oscillatory sheet flow for well sorted and graded sands. Coast. Eng. 50 (3), 117–138. http://dx.doi.org/10.1016/j.coastaleng.2003.09.004.
Peregrine, D.H., 1983. Breaking waves on beaches. Annu. Rev. Fluid Mech. 15 (1), 149–178. http://dx.doi.org/10.1146/annurev.fl.15.010183.001053.
Price, T.D., Ruessink, B.G., 2011. State dynamics of a double sandbar system. Cont. Shelf Res. 31 (6), 659–674. http://dx.doi.org/10.1016/j.csr.2010.12.018.
Reniers, A.J.H.M., Gallagher, E.L., MacMahan, J.H., Brown, J.A., van Rooijen, A.A., de Vries, J.S.M.V., van Prooijen, B.C., 2013. Observations and modeling of steep-beach grain-size variability. J. Geophys. Res. Oceans 118 (2), 577–591. http://dx.doi.org/10.1029/2012jc008073.
Ribberink, J.S., 1998. Bed-load transport for steady flows and unsteady oscillatory flows. Coast. Eng. 34, 59–82.
Ribberink, J.S., Al-Salem, A.A., 1994. Sediment transport in oscillatory boundary layers in cases of rippled beds and sheet flow. J. Geophys. Res. 99 (C6), 12707–12727. http://dx.doi.org/10.1029/94jc00380.
Ribberink, J.S., Al-Salem, A.A., 1995. Sheet flow and suspension of sand in oscillatory boundary-layers. Coast. Eng. 25 (3–4), 205–225. http://dx.doi.org/10.1016/0378-3839(95)00003-T.
Ribberink, J.S., van der Werf, J.J., O'Donoghue, T., Hassan, W.N.M., 2008. Sand motion induced by oscillatory flows: sheet flow and vortex ripples. J. Turbul. 9 (20), 1–32. http://dx.doi.org/10.1080/14685240802220009.
Richmond, B.M., Sallenger, A.H., 1984. Cross-shore transport of bimodal sands. In: Proc. Coastal Engineering Conference: 1997-2008.
Roelvink, J.A., Reniers, A., 1995. LIP 11D Delta Flume Experiments - Data Report. W. D. Hydraulics. Delft, The Netherlands, p. 124.
Ruessink, B.G., Kuriyama, Y., Reniers, A.J.H.M., Roelvink, J.A., Walstra, D.J.R., 2007. Modeling cross-shore sandbar behavior on the timescale of weeks. J. Geophys. Res. 112 (F3) http://dx.doi.org/10.1029/2006jf000730.
Ruessink, B.G., Michallet, H., Abreu, T., Sancho, F., Van der A, D.A., Van der Werf, J.J., Silva, P.A., 2011. Observations of velocities, sand concentrations, and fluxes under velocity-asymmetric oscillatory flows. J. Geophys. Res. 116 (C3) http://dx.doi.org/10.1029/2010jc006443.
Sallenger, A.H., Holman, R.A., Birkemeier, W.A., 1985. Storm-induced response of a nearshore-bar system. Mar. Geol. 64, 237–257.
Schretlen, J.L.M., 2012. Sand Transport under Full-scale Progressive Surface Waves. PhD Thesis. University of Twente, The Netherlands.
Sistermans, P.G.J., 2002. Graded Sediment Transport by Non-breaking Waves and Currents. PhD thesis, TU Delft, the Netherlands.
Sleath, J.F.A., 1999. Conditions for plug formation in oscillatory flow. Cont. Shelf Res. 19 (13), 1643–1664. http://dx.doi.org/10.1016/s0278-4343(98)00096-x.
Smith, E.R., Kraus, N.C., 1991. Laboratory study of wave-breaking over bars and artificial Reefs. J. Waterw. Port Coast. Ocean Eng. 117 (4), 307–325. http://dx.doi.org/10.1061/(asce)0733-950x(1991)117:4(307).
Srisuwan, C., Work, P.A., 2015. Beach profile model with size-selective sediment transport. II: numerical modeling. J. Waterw. Port Coast. Ocean Eng. 141 (2) http://dx.doi.org/10.1061/(asce)ww.1943-5460.0000274, 04014033.
Srisuwan, C., Work, P.A., Karasu, S., Özölçer, İ.H., 2015. Beach profile model with size-selective sediment transport. I: laboratory experiment and sensitivity study. J. Waterw. Port Coast. Ocean Eng. 141 (2) http://dx.doi.org/10.1061/(asce)ww.1943-5460.0000255, 04014032.
Sumer, B.M., Chua, L.H.C., Cheng, N.S., Fredsoe, J., 2003. Influence of turbulence on bed load sediment transport. J. Hydraul. Eng. ASCE 129 (8), 585–596. http://dx.doi.org/10.1061/(Asce)0733-9429(2003)129:8(585).
Sumer, B.M., Guner, H.A.A., Hansen, N.M., Fuhrman, D.R., Fredsøe, J., 2013. Laboratory observations of flow and sediment transport induced by plunging regular waves. J. Geophys. Res. Oceans 118 (11), 6161–6182. http://dx.doi.org/10.1002/2013jc009324.
Sumer, B.M., Kozakiewicz, A., Fredsoe, J., Deigaard, R., 1996. Velocity and concentration profiles in sheet-flow layer of movable bed. J. Hydraul. Eng. 122 (10), 549–558. http://dx.doi.org/10.1061/(asce)0733-9429(1996)122:10(549).
Svendsen, I.A., Madsen, P.A., Buhr Hansen, J., 1978. Wave characteristics in the surf zone. In: Proc. 16th Conf. Coastal Eng. Hamburg, Germany. American Society of Civil Engineers, pp. 520–539.
Swart, D.H., 1974. Offshore Sediment Transport and Equilibrium Beach Profiles. PhD Thesis, TU Delft.
Thornton, E.B., Humiston, R.T., Birkemeier, W., 1996. Bar/trough generation on a natural beach. J. Geophys. Res. Oceans 101 (C5), 12097–12110. http://dx.doi.org/10.1029/96jc00209.
van der A, D.A., O'Donoghue, T., Ribberink, J.S., 2009. Sheet flow sand transport processes in oscillatory flow with acceleration skewness. In: Proc. Coastal Sediments 2009. World Scientific, Singapore.
van der A, D.A., O'Donoghue, T., Ribberink, J.S., 2010. Measurements of sheet flow transport in acceleration-skewed oscillatory flow and comparison with practical formulations. Coast. Eng. 57 (3), 331–342. http://dx.doi.org/10.1016/j.coastaleng.2009.11.006.
van der A, D.A., O'Donoghue, T., Davies, A.G., Ribberink, J.S., 2011. Experimental study of the turbulent boundary layer in acceleration-skewed oscillatory flow. J. Fluid Mech. 684, 251–283. http://dx.doi.org/10.1017/jfm.2011.300.
van der A, D.A., Ribberink, J.S., van der Werf, J.J., O'Donoghue, T., Buijsrogge, R.H., Kranenburg, W.M., 2013. Practical sand transport formula for non-breaking waves and currents. Coast. Eng. 76, 26–42. http://dx.doi.org/10.1016/j.coastaleng.2013.01.007.
van der, A.D.A., van der Zanden, J., O'Donoghue, T., Hurther, D., Cáceres, I., McLelland, S.J., Ribberink, J.S., 2017. Large-scale laboratory study of breaking wave hydrodynamics over a fixed bar. J. Geophys. Res. Oceans 122 (4), 3287–3310. http://dx.doi.org/10.1002/2016jc012072.
van der Werf, J.J., Schretlen, J.J.L.M., Ribberink, J.S., O'Donoghue, T., 2009. Database of full-scale laboratory experiments on wave-driven sand transport processes. Coast. Eng. 56 (7), 726–732. http://dx.doi.org/10.1016/j.coastaleng.2009.01.008.
van der Werf, J.J., Veen, R., Ribberink, J.S., van der Zanden, J., 2015. Testing of the new SANTOSS transport formula in the Delft3D morphological modeling system. In: Proceedings of Coastal Sediments, San Diego, USA, p. 14.
van der Zanden, J., Alsina, J.M., Cáceres, I., Buijsrogge, R.H., Ribberink, J.S., 2015a. Bed level motions and sheet flow processes in the swash zone: observations with a new conductivity-based concentration measuring technique (CCM+). Coast. Eng. 105, 47–65. http://dx.doi.org/10.1016/j.coastaleng.2015.08.009.
van der Zanden, J., Van der A, D.A., Ribberink, J.S., O'Donoghue, T., Hurther, D., Caceres, I., Thorne, P.D., 2015b. Sand transport process measurements under large-scale breaking waves. In: Proc. Coastal Sediments, San Diego, USA, p. 14.
van der Zanden, J., van der A, D.A., Hurther, D., Cáceres, I., O'Donoghue, T., Ribberink, J.S., 2016. Near-bed hydrodynamics and turbulence below a large-scale plunging breaking wave over a mobile barred bed profile. J. Geophys. Res. Oceans 121 (8), 6482–6506. http://dx.doi.org/10.1002/2016jc011909.
van der Zanden, J., Van der A, D.A., Hurther, D., Caceres, I., O'Donoghue, T., Ribberink, J.S., 2017. Suspended sediment transport around a large-scale laboratory breaker bar. Coast. Eng. 125, 51–69. http://dx.doi.org/10.1016/j.coastaleng.2017.03.007.
Van Rijn, L.C., 1998. The effect of sediment composition on cross-shore bed profiles. In: Proc. 26th Int. Conf. on Coastal Engineering, pp. 2495–2508.
van Rijn, L.C., 2007. Unified view of sediment transport by currents and waves. III: graded beds. J. Hydraul. Eng. ASCE 133 (7), 761–775. http://dx.doi.org/10.1061/(Asce)0733-9429(2007)133:7(761).
van Rijn, L.C., Ribberink, J.S., van der Werf, J.J., Walstra, D.J.R., 2013. Coastal sediment dynamics: recent advances and future research needs. J. Hydraul. Res. 51 (5), 475–493. http://dx.doi.org/10.1080/00221686.2013.849297.
Wang, P., Davis, R.A., Kraus, N.C., 1998. Cross-shore distribution of sediment texture under breaking waves along low-wave-energy coasts. J. Sediment. Res. 68 (3), 467–506.
Watanabe, A., Sato, S., 2004. A sheet-flow transport rate for asymmetric, forward-leaning waves and currents. In: Proceedings 29th International Conference on Coastal Engineering, vol. 2. World Scientific, pp. 1703–1714.
Wiberg, P.L., Drake, D.E., Cacchione, D.A., 1994. Sediment resuspension and bed armoring during high bottom stress events on the northern California inner continental shelf: measurements and predictions. Cont. Shelf Res. 14 (10–11), 1191–1219. http://dx.doi.org/10.1016/0278-4343(94)90034-5.
Wijnberg, K.M., Kroon, A., 2002. Barred beaches. Geomorphology 48 (1–3), 103–120. http://dx.doi.org/10.1016/S0169-555x(02)00177-0.
Wright, L.D., Short, A.D., 1984. Morphodynamic variability of surf zones and beaches - a synthesis. Mar. Geol. 56 (1–4), 93–118. http://dx.doi.org/10.1016/0025-3227(84)90008-2.
Zala Flores, N., Sleath, J.F.A., 1998. Mobile layer in oscillatory sheet flow. J. Geophys. Res. Oceans 103 (C6), 12783–12793. http://dx.doi.org/10.1029/98jc00691.
Zhang, D.P., Sunamura, T., 1994. Multiple bar formation by breaker-induced vortices: a laboratory approach. In: Proc. Intern. Conf. Coast. Eng., pp. 2856–2870.